Journal of Materials Chemistry A

ROYAL SOCIETY OF CHEMISTRY

PERSPECTIVE

View Article Online
View Journal | View Issue

Cite this: J. Mater. Chem. A, 2022, 10, 19534

Chemically functionalized phosphorenes and their use in the water splitting reaction

Pratap Vishnoi, * Aditi Saraswat and C. N. R. Rao *

In the last 7 years, phosphorene (or few layer black phosphorus) has emerged as not only a superior optoelectronic material, but also a potential catalyst for the hydrogen evolution reaction (HER) from water splitting owing to its thickness dependent bandgap, broad spectrum light absorption, high charge-carrier mobility, and high density of surface-active sites. However, pristine phosphorene produces trace amounts of H_2 primarily due to its poor ambient stability and a large positive change in the Gibbs free energy of hydrogen (H*) adsorption/desorption ($\Delta G_{H^*} > 0$). Due to the recent surge of interest in metal-free HER catalysts, there have been many successful efforts on enhancing the stability as well as the catalytic activity of phosphorene through chemical functionalization, metal doping, and 2D heterocomposites. In this perspective, we present different types of interactions, including covalent, coordination, electrostatic, van der Waals, charge-transfer, and interfacial, which have been utilized in preparing modified phosphorenes. Then, we assess the noteworthy properties of phosphorene, which make it an efficient HER catalyst and discuss the developments in photocatalytic, electrocatalytic, and photo-electrocatalytic means of H_2 production using phosphorene based catalysts. We conclude the perspective with suggestions for exciting future developments.

Received 11th March 2022
Accepted 3rd June 2022

DOI: 10.1039/d2ta01932a

rsc.li/materials-a

1. Introduction

Heterogeneous catalysis of the hydrogen evolution reaction (HER) by water splitting ($H_2O \rightarrow H_2 + \frac{1}{2}O_2$; $\Delta G^o = +237$ kJ mol^{-1}) is deemed to be a prospective solution for the energy crisis and detrimental environmental effects caused by burning fossil

New Chemistry Unit, School of Advanced Materials, International Centre for Materials Science, Jawaharlal Nehru Centre for Advanced Scientific Research (JNCASR), Jakkur, Bangalore, 560064, India. E-mail: pvishnoi@jncasr.ac.in; cnrrao@jncasr.ac.in

Pratap Vishnoi is a Ramanujan faculty fellow at the Jawaharlal Nehru Centre for Advanced Scientific Research (JNCASR), Bangalore. He received his Ph. D. in chemistry from the Indian Institute of Technology Bombay (IIT Bombay) under the supervision of Prof. R. Murugavel. He then worked as a post-doctoral fellow at the JNCASR with Prof. C. N. R. Rao and subsequently at the University of California Santa Barbara (UCSB) with Prof. Ram Seshadri and Prof. Sir Anthony K. Cheetham. His current research interests are in multifunctional hybrid organic-inorganic materials, halide perovskites and layered nanomaterials.

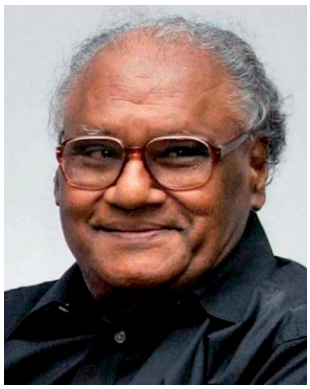

C. N. R. Rao is the Linus Pauling Research Professor at the JNCASR, Bangalore and Honorary Professor at the Indian Institute of Science, Bangalore. He is the member of several scientific academies, including the Royal Society and the US National Academy of Sciences. He is the recipient of several prestigious awards, including the Royal Medal of the Royal Society, the Dan David Prize, Illy Trieste Science Prize, the August von Wilhelm Hoffmann medal of the German Chemical Society, the von Hippel Award of the Materials Research Society, Eni International Award for Research in Energy Frontiers and Sheikh Saud International Prize for Materials Science. His research interests are in the chemistry of materials, especially 2D materials and their chemical functionalization, reduction of water and CO_2 and aliovalent substitution.

fuels. Among numerous materials, which have been identified as the potential HER catalysts after decades of research, state-of-the-art Pt and Pt group metals have remained the best performing catalyst.[1,2] However, the applicability of Pt based systems is limited by their high cost, limited availability, and lack of tolerance to catalyst poisoning.[3] To reduce and hopefully eliminate the dependence on metal-based catalysts, there is a surge of interest in catalysts comprising non-metal and earth abundant elements, such as B, C, N, and P. For example, carbon nitride,[4] doped graphene, and graphene hybrids,[4,5] borocarbonitrides,[3] and phosphorene (few layer black phosphorus)[6] hold promise for efficient HER catalysts.

Phosphorene is the isolated monolayer of black phosphorus (BP), in a similar way as graphene is the isolated monolayer of graphite. It was first obtained in 2014 from the exfoliation of BP crystals.[7] During the last 7 years, it has witnessed a major renaissance in a range of applications, including in transistor,[8] photodetector,[9] gas sensor,[10] and catalysis.[11] Perhaps, the HER catalysis is one of the most intriguing applications of phosphorene. Phosphorene has a thickness dependent bandgap of 0.3 eV (bulk) to 2.0 eV (monolayer), wide spectrum light absorption capability, high charge carrier mobility, efficient electron–hole separation, and high density of exposed active sites.[7,12] Its conduction band lies at an appropriate energy level for the HER, *i.e.* water reduction.[13] However, its inherent HER activity is rather poor, mainly due to ambient instability and a large positive change in the Gibbs free energy of adsorption/desorption for hydrogen intermediate state ($\Delta G_{H^*} > 0$).[14] The instability is caused by the reactive nature of non-bonding lone pair electrons (LPEs) in phosphorus. The other side of the coin is that the LPEs can be utilized non-destructively in chemical functionalization, which not only protects phosphorene against ambient decomposition but also reduces its ΔG_{H^*}. Furthermore, phosphorene based composites have been identified as potential photocatalysts for CO_2 reduction.[15,16] Among the emerging CO_2 conversion techniques, semiconductor based photocatalysis gives rise advantages of utilizing renewable solar energy as well as forming value added chemicals including CO, CH_4, and CH_3OH.[17]

Few-layer black phosphorus/phosphorene and its composites have emerged as leading metal-free HER catalysts ever since the first report in 2016.[18] The number of publications has remarkably increased (Fig. 1). In recent reviews, the HER application of phosphorene has been summarized along with vastly different topics, including synthetic methods, fundamental properties, and diverse applications.[19–21] In this perspective, we provide the highlights of phosphorene based electrocatalysis, photocatalysis, and photo-electrocatalysis of H_2 evolution. We start with a brief overview of the fundamental properties of phosphorene and present the key developments on its ambient stabilization through chemical functionalization and 2D-heterostructures. Then, we discuss the developments in H_2 production by phosphorene-based catalysts and highlight how they show superior activities, in some cases even close to that of state-of-the-art Pt and Pt group metals. We also provide suggestions for future opportunities.

2. History and renaissance

The history of phosphorene traces back to 1914 when Bridgman synthesized BP, whilst studying high pressure phase transition in white phosphorus.[22] For a century, between 1914 and 2014, the work on BP progressed steadily on its structural,[23] electric transport,[24] and superconductivity aspects.[25] Inspired by the discovery of graphene from graphite in 2004,[26] and its extraordinary transport properties revealed afterwards, the semiconductor research community has explored the exfoliation of many other existing layered materials into their nanosheets. In

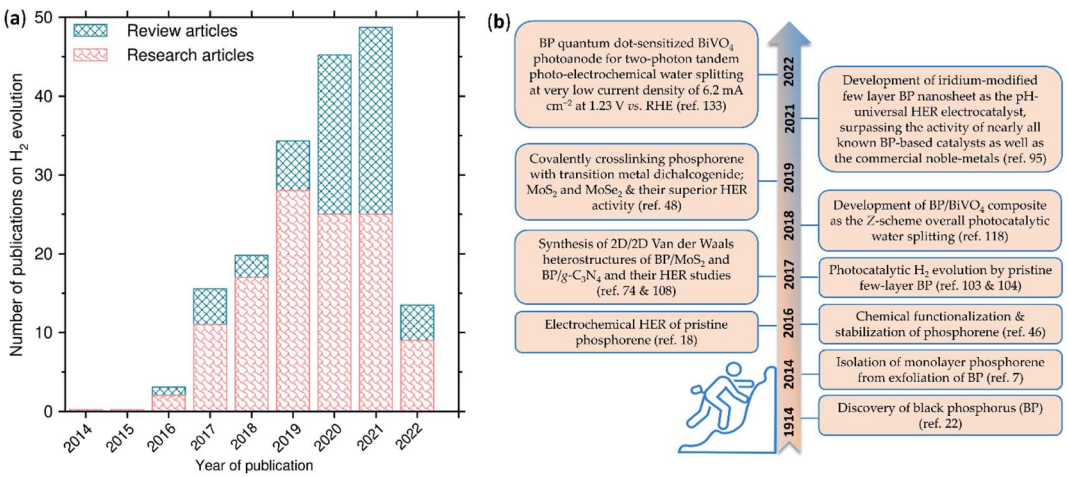

Fig. 1 (a) Number of research publications on few-layer phosphorus/phosphorene based H_2 evolution catalysts. The publications were obtained from web of science on May 06, 2022, with the search keywords combinations of either "phosphorene" and "hydrogen", "black phosphorus" and "hydrogen" or "black phosphorene" and "hydrogen". Only those research articles have been included which show experimental reports on H_2 evolution from water splitting, whilst purely theoretical reports have been excluded. Only those review articles have been included in which experimental results on HER have been summarized. (b) A timeline of the key milestone developments of few-layer black phosphorus/phosphorene based HER catalysts.

2014, Liu *et al.*[7] isolated monolayer phosphorene from scotch tape exfoliation of BP crystal, which captured wide research attention. Since then, phosphorene has seen a major renaissance in nanoscience and nanotechnology. This has also led to a revival of the interest in the bulk properties of BP.[27,28]

3. Crystal structure

BP has three pressure dependent polymorphs at room temperature:[27] (1) semiconducting orthorhombic phase (A17, *Cmca*) at the ambient pressure, (2) semimetallic rhombohedral phase (A7, $R\bar{3}m$) at $5 < P < 11$ GPa, and (3) metallic simple cubic phase (sc, $Pm\bar{3}m$) at ≥ 11 GPa. The orthorhombic phase is the thermodynamically most stable form among all the allotropes of phosphorus. It has a buckled layered structure with covalent P–P bond within the layer and weak van der Waals interaction between the layers (Fig. 2a).[29] The layers stack along the *b*-axis at a distance of 5.23 Å. Each monolayer is a bilayer of two parallel atomic planes comprising sp^3 hybridized P atoms. Due to sp^3 hybridization, phosphorene adopts a puckered structure, unlike graphene, which is an atomically flat layer of sp^2 carbon. The puckered arrangement of atoms makes phosphorene sheet strongly anisotropic along the armchair and the zigzag directions, corresponding to the *x*-direction (*c*-axis) and *y*-direction (*a*-axis), respectively (Fig. 2b).[30] Three of the five valence electrons in phosphorus form the covalent P–P bonds, whilst two remain as the non-bonding lone pair (Fig. 2c and d). Due to puckering, the sheet shows structural anisotropy with smaller P–P distances and ∠P–P–P angles along the zigzag directions compared to those along the armchair direction. Many of the properties of phosphorene, including optical absorption,[31] emission,[32] thermal conductivity,[33] and electric conductivity[7] differ along these two directions. Further, the interlayer P–P distance of 3.60 Å suggests that there is a weak van der Waals interaction between the layers, which allows easy exfoliation of BP crystals into thin nanosheets.[12] BP crystals can be exfoliated by liquid,[34] mechanical,[7] and electrochemical methods.[35]

4. Electronic band structure

The electronic structure and properties of phosphorene have been extensively studied by optical absorption,[34] photoluminescence,[7,36] and DFT calculations.[37] It exhibits a direct bandgap regardless of the thickness, unlike indirect to direct band crossover in transition metal dichalcogenides when exfoliating their bulk crystals into monolayer materials.[38] The direct band nature of bulk BP has been experimentally confirmed from the angle-resolved photoemission spectroscopy (ARPES) measurements.[8] On increasing the number of layers, the bandgap gradually decreases from ~2.0 eV to ~0.30 eV (Fig. 2e).[37] It has been suggested that the interlayer van der Waals interaction plays an important role in the layer-dependence of the bandgap. Stronger interaction causes a wider band dispersion and a narrower bandgap with concomitant splitting of the bands as reflected in the band structure of 2L and 3L phosphorene (Fig. 2e).[37] The band dispersion is anisotropic along the Γ–X (corresponding to the armchair direction) and Γ–Y (corresponding to the zigzag direction) directions.[31] Wide bandgap tuneability along with the anisotropic behaviour of electrons, photons, and phonons

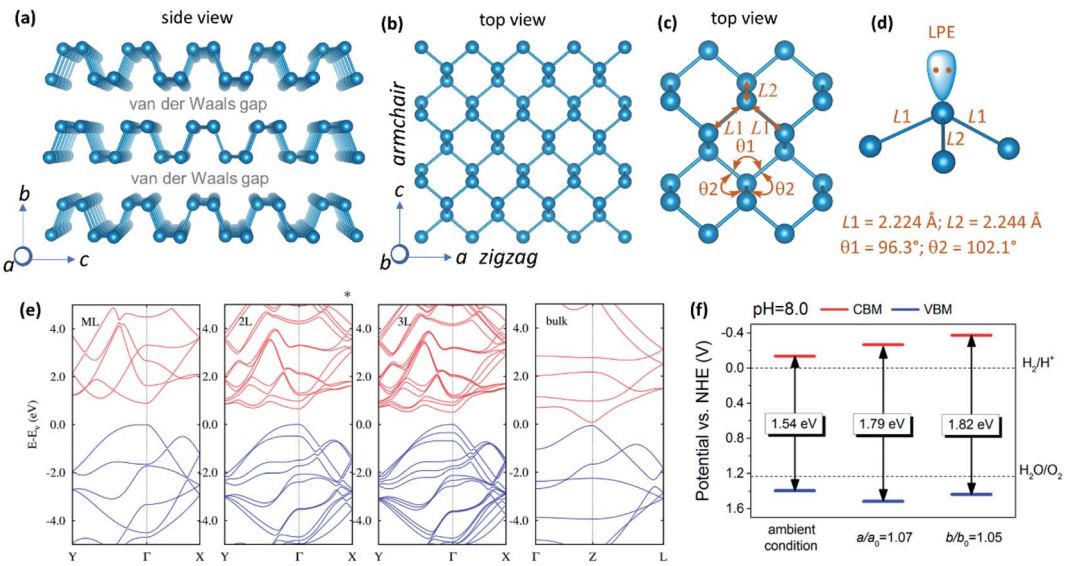

Fig. 2 (a) Crystal structure of BP drawn from the crystal information file (CIF) reported elsewhere (orthorhombic *Cmca* space group; $a = 3.3136$ Å, $b = 10.4788$ Å and $c = 4.3763$ Å; $Z = 8$).[29] (b) Structure of phosphorene sheet showing armchair and zigzag directions. (c) A portion of phosphorene sheet showing P–P bonds and ∠P–P–P angles. (d) Phosphorus atom showing three P–P bonds and a non-bonding lone pair electron. (e) Calculated band structures of monolayer (ML), bilayer (2L), trilayer (3L), and bulk BP. The occupied and unoccupied bands are shown in blue and red, respectively. (f) Calculated (using HSE06 functional) relative energy levels of the conduction and the valance bands of phosphorene under 5% tensile strain along the armchair direction and under 7% tensile strain along the zigzag direction at pH 8.0. Panel (e) is reproduced with permission from ref. 37, © 2014 American Physical Society. Panel (f) is reproduced with permission from ref. 13, © 2014 American Chemical Society.

make phosphorene a promising material for optoelectronics and related applications. Below are the unique aspects of the electronic structure of phosphorene that favour the HER catalysis: (i) Thickness dependent bandgap: the thickness tuneable bandgap makes phosphorene an excellent material for absorbing photons in the visible and the near-infrared regions of the electromagnetic spectrum to effectively generate excited electrons and holes. (ii) High carrier mobility: conductivity is a prerequisite for photocatalysis and electrocatalysis. Due to high charge carrier mobility, phosphorene exhibits effective separation of charge carriers, and their migration to the catalyst surface. (iii) Band position: calculations have suggested that conduction band minima (CBM) and valence band maxima (VBM) of unstrained phosphorene lie above the required potential for the water reduction reaction ($2H^+ + 2e^- \rightarrow H_2$; $E^0 =$ 0.0 V *vs.* NHE at pH = 7) as well as the water oxidation reaction ($H_2O \rightarrow \frac{1}{2}O_2 + 2e^-$; $E^0 = +1.23$ V *vs.* NHE at pH = 7),[13,39] (NHE = normal hydrogen electrode), making it suitable for HER catalysis in the presence of a hole scavenger. The utility of phosphorene as a photocatalytic oxygen evolution reaction (OER) is limited. However, at a slightly high pH of 8.0 and intraplanar strain, CBM and VBM of phosphorene straddle the water reduction and oxidation potentials (Fig. 2f),[13] thereby making it suitable for overall water splitting.

5. Ambient degradation and protection

Although phosphorene is thermodynamically stable, it is chemically unstable due to the reactive nature of LPEs. Under ambient conditions, phosphorene can form P–O and P═O moieties on its surface by reacting with oxygen.[40–42] These surface moieties then absorb water molecules and eventually lead to the oxidation of the phosphorene sheet. In oxygenated water, phosphorene decomposes into water soluble acids, including H_3PO_2, H_3PO_3, and H_3PO_4 as the major products, and the decomposition preferentially occurs on the edges.[43] Furthermore, visible light irradiation promotes the decomposition process.[44,45] Ambient decomposition suppresses the electronic and the physical properties of phosphorene, which is a major bottleneck for its real-time applications, including HER. Regardless of the instability, the LPEs in phosphorus provide plenty of opportunities to non-destructively interact with a range of electron accepting functionalities through covalent and noncovalent interactions. The functional groups are expected to reduce the LPE density on the phosphorene surface and suppress its reactivity towards oxygen. Furthermore, the functional groups provide shielding against direct contact with reactive species in the ambience and enhance the stability as well as many of the useful properties of phosphorene. Fig. 3 shows various types of interactions, which have been employed for phosphorene functionalization.

5.1. By covalent interaction

The LPE can form covalent bonds, P–X (X = C, Si, N or O), with appropriate functional groups. Ryder *et al.*[46] have reacted BP nanosheets of ~10 nm thickness with aryl diazonium salts to attach aryl groups through P–C bonds, which not only stabilized BP under the ambient conditions, but also improved the carrier mobility through p-type doping. The functionalized phosphorus adopts four-coordinate bonding, in a similar way as molecular phosphines form phosphonium compounds with aryl diazonium salts.[47] Rao and coworkers[48] have synthesized phosphorene ylide from the reaction of liquid exfoliated phosphorene

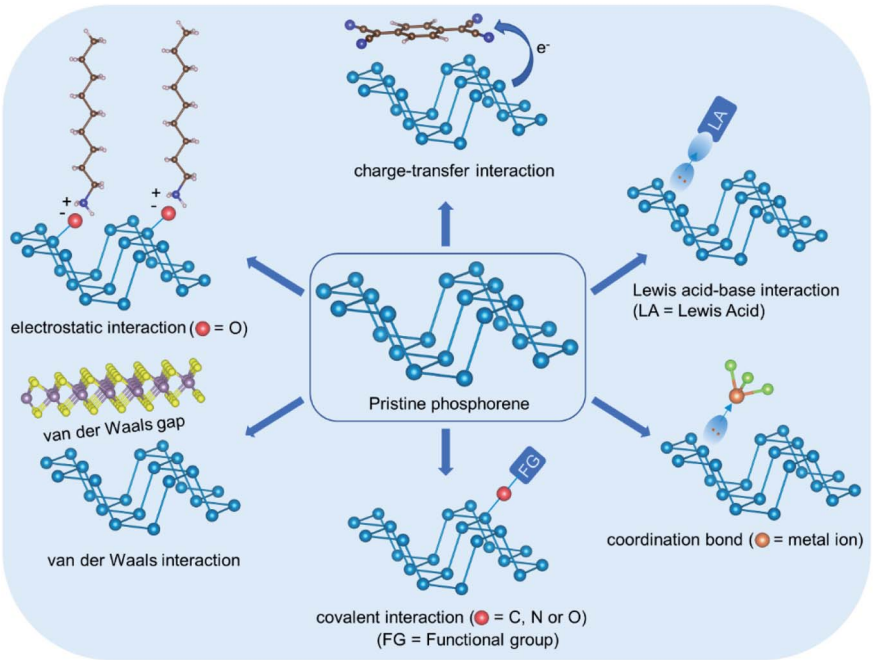

Fig. 3 Schematic overview of various types of interactions employed in phosphorene functionalization.

with benzyl bromide. The resultant ylide has been reacted with an aldehyde to form alkene *via* a Wittig type of reaction. Although P–C bonds firmly hold the functional groups on phosphorene, the four-coordinate phosphorus remains coordinatively unsaturated, due to which an optimal degree of functionalization still cannot be reached. Under ultraviolet (UV) light irradiation, phosphorene has been functionalized with organic azides ($R–N_3$) through P=N bonds wherein the functionalized phosphorus atoms are five-coordinated.[49,50] The UV light induces the formation of reactive nitrene species from azide, which then attach to phosphorene sheets through P=N bonds. Due to five-coordinate bonding, the reactivity of phosphorene towards oxygen reduces significantly, leading to much better ambient stability. Amino ($–NH_2$) functionalized BP nanosheets have been synthesised by ball milling BP crystals with urea, which simultaneously enhances the stability and the HER activity.[51] Other studies have shown that hydroxyl groups formed on partially oxidized phosphorene can react with alkyl alcohol (R–OH)[52] and trimethylsilyl chloride (TMS–Cl)[53] to form P–OR and P–OSi bonds, respectively. The covalent interaction has also been adopted as an efficient strategy to form 2D heterostructures of phosphorene with other important layered materials, such as MoX_2 (X = S or Se),[48] and *g*-C_3N_4.[54]

5.2. By forming Lewis acid–base complex

Phosphorene acts as a Lewis base due to the LPEs, and it can, therefore, interact with Lewis acid (LA), just like molecular phosphines.[55] The Lewis acid–base interaction is expected to make LPEs inaccessible to oxygen.[56] Rao and coworkers have reported the adducts of phosphorene with $B(C_6F_5)_3$ and $InCl_3$. $B(C_6F_5)_3$ gives rise to better protection owing to stronger electrophilicity and sterical hindrance.[11] A recent study on a series of LAs including BBr_3, $B(C_6F_5)_3$, BPh_3, $Al(OCOR)_3$, $Al(O^sBu)_3$, $AlCl_3$, $AlBr_3$, and $GaCl_3$ has revealed that electrophilicity, steric hindrance, and Pearson hard/soft-ness can be used as the key parameters to qualitatively access the stability of the functionalized phosphorene.[57] Highly electrophilic $AlCl_3$, $AlBr_3$, and $GaCl_3$ provide better protection and also cause p-type doping of phosphorene.[57]

5.3. By forming coordinating bonds

Metals with empty or partially filled d- or f-orbitals show strong electron affinity and can, therefore, coordinatively bind with phosphorene LPEs. For example, coordinatively unsaturated TiL_4 (L = *p*-toluenesulfonate),[58] LnL_3 (Ln = Tb, Eu or Nd; L = trifluoromethanesulfonate)[59] have been reported to coordinatively interact with phosphorene. The functionalized phosphorenes show excellent stability in air and water. In addition, the lanthanide tagged phosphorenes can potentially be used as contrast agents in magnetic resonance imaging (MRI). Furthermore, the sulfonate ligands strengthen the coordinating ability of metal ions. Ir-complex[60] and cisplatin[61] have also been attached to phosphorene, and the resultant phosphorenes have been examined as drug delivery agents.

Further, phosphorene has been functionalized with chemically adsorbed metal atoms or ions, called adatom. Using sputtered deposition, Cu atoms have been deposited on phosphorene surface and interstitial.[62] At both locations, each Cu transfers one electron to phosphorene and oxidizes into a more stable Cu^+ state (d^{10}). Thus, the Cu modified phosphorene behaves as an n-type semiconductor, with a remarkable increase in electron mobility from 380 $cm^2 V^{-1} s^{-1}$ at 300 K to 2140 $cm^2 V^{-1} s^{-1}$ at 7 K. While there is no experimental report on direct deposition of Cu^+ on phosphorene, but Ag^+ adatom has been achieved *via* cation–π interactions, which causes p-type doping of phosphorene with the room temperature hole mobility increasing from 796 $cm^2 V^{-1} s^{-1}$ to 1593 $cm^2 V^{-1} s^{-1}$.[63] It was proposed that Ag^+ ion interacts with three distinct LPEs through η^3-coordination. Noble metals such as dipallada unit (Pd_2) have been sandwiched between phosphorene sheets.[64] The extended X-ray absorption fine structure (EXAFS) analysis and the DFT modelling have highlighted that the coordination of Pd_2 occurs between the layer, bridging two phosphorene sheets.

5.4. By charge transfer interaction

Electron withdrawing organic molecules, such as 7,7,8,8-tetracyano-*p*-quinodimethane (TCNQ)[65] and tetracyanoethylene (TCNE),[66] accept electrons from *phosphorene and form* charge transfer (CT) interaction. It has been found that the Raman scattering of phosphorene is sensitive to charge doping.[66] It has three Raman modes (*i.e.*, A_{1g}, B_{2g} and A_{2g}) and all of which show softening and broadening on hole and electron doping, with the former causing stronger effects. TCNQ and TCNE have been utilized for hole doping, whilst tetrathiafulvalene (TTF) for electron doping.[66] Further, the interactions of TCNQ, TCNE, and TTF with phosphorene have been studied through quenching the photoluminescence of phosphorene quantum dots (PQDs).[67] Among these molecules, TCNQ most efficiently quenches the photoluminescence as indicated by the Stern–Volmer constants ($K_{sv} = 7.0 \times 10^4$ M^{-1}, 1.0×10^4 M^{-1}, and 6.6×10^3 M^{-1} for TCNQ, TCNE, and TTF, respectively[67]). This trend is consistent with their electron withdrawing nature as has been confirmed by the Bader charge-population analysis.[68] Furthermore, the electron withdrawing molecules not only reduce the electron density on the phosphorene surface, but also trap the photogenerated electrons, which otherwise cause oxidative decomposition of phosphorene.[69]

5.5. By electrostatic interaction

The phosphorene electron density can interact with cationic organic molecules through electrostatic interaction. For example, ionic liquids (1-butyl-3-methylimidazolium tetrafluoroborate),[40] surfactants with long hydrophobic chains and small hydrophilic headgroups (cetyltrimethylammonium bromide),[70] and long chain alkyl ammonium cation could be effectively utilized.[71] In addition, the vertical packing of long alkyl chains creates an additional physical barrier on the phosphorene surface for oxygen and water.

5.6. By van der Waals interaction

Organic molecules with extended π-electrons cloud, such as 3,4,9,10-perylene-tetracarboxylic-dianhydride (PTCDA)[72] and anthraquinone (AQ)[73] show very small charge-transfer to/from

phosphorene and adsorb mostly *via* van der Waals interaction. van der Waals interaction has also been exploited in 2D/2D heterostructures of phosphorene with other important layered materials such as MoS_2.[74]

Covalent functionalization is no doubt an effective approach to functionalize and generate different materials with improved properties, such as covalently cross-linked 2D/2D heterostructures. However, in the case of phosphorene, sometimes the covalent functionalization suffers from a few drawbacks: (i) low degree of functionalization due to low reactivity of neutral phosphorene,[75,76] and (ii) P–P bond breaking as a consequence of covalent bond formation with the functional groups, which has detrimental effects on the properties.[75] On the other hand, non-covalent functionalization protects phosphorene with little (or no) distortion of the lattice, provides a relatively higher degree of functionalization, and preserves most of its properties. Many of the phosphorene-based composite HER catalysts utilize the non-covalent interactions to effectively tune interfacial charge transfer and charge carrier separation.

6. HER catalysts based on phosphorene

6.1. Mechanism of water splitting

Water splitting is an uphill reaction with a positive change in the Gibbs free energy (ΔG^o) of +237 kJ mol^{-1} (equivalent to a potential difference of 1.23 V between anode and cathode or the energy demand of 1.23 eV per electron–hole pair generated). In the electrochemical process, HER occurs at the cathode through the reduction half reaction ($2H^+ + 2e^- \rightarrow H_2$; $E^0 = 0.0$ V *vs.* NHE at pH = 7), while the oxidation half reaction ($H_2O \rightarrow \frac{1}{2}O_2 + 2e^-$; $E^0 = +1.23$ V *vs.* NHE at pH = 7) occurs at the anode (Fig. 4a). Experimentally, the potential requirement for electrolysis of water is >1.23 V. This excess potential is required to account for the overpotential caused by the large activation barrier. A semiconductor with a bandgap of more than 1.23 eV can absorb radiation of wavelength less than 1000 nm and becomes photo excited (Fig. 4b). The photogenerated electrons (e^-) can reduce water into H_2 if the conduction band minima (CBM) of the semiconductor lies at a more negative potential than water reduction potential, whilst the holes (h^+) can oxidize water into O_2 if the valence band maxima (VBM) of semiconductor lies at a more positive potential than the water oxidation potential. Experimentally, the energy requirement for the photocatalytic process is much more than 1.23 eV and is, generally, in the range of 1.6–2.4 eV per electron–hole pair generated.[77] This excess energy accounts for the additional energy required to overcome the activation energy barrier.

A good HER catalyst reduces the activation barrier by enabling adsorption and desorption of the intermediate adsorbed state (H*) on its active sites while keeping the overall process thermoneutral ($|\Delta G_H^*| = 0$).[78] DFT calculations have suggested that the basal plane of a perfect phosphorene nanosheet has a large positive ΔG_H^* of 1.25 eV,[79] which makes it inherently poor HER catalyst. However, its activity can be boosted by introducing point defects such as Stone–Wales and vacancy defects.[14,79] The phosphorus atoms present at the odd size vacancies (*i.e.* monoatomic or triatomic) as well as at the edge sites are much more HER active when compared to those present at the even size vacancies (*i.e.* divacancy).[14] The atomic vacancies induce a strain field and bond deformation around the defect core, which enhances HER activity through effective hydrogen–phosphorus interaction. There exists a few experimental reports, which suggest that HER activity of phosphorene is indeed higher at its defect and edge sites.[18,79]

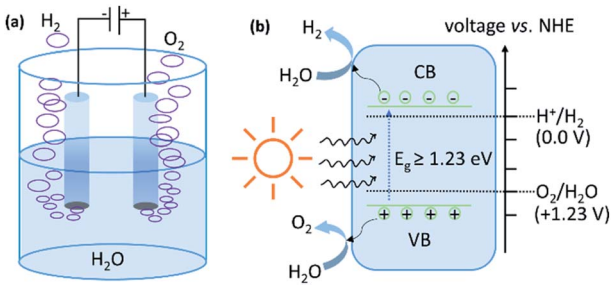

Fig. 4 Schematic illustration of the mechanism of water splitting by (a) electrocatalytic (b) photocatalytic routes.

6.2. Electrocatalysis

Phosphorene based HER electrocatalysts have shown activities ranging from very low to high, and in some cases even surpassing the commercial Pt/C catalyst. Experimentally, the electrochemical HER figure of merit is estimated by the overpotential with respect to a reversible hydrogen electrode (RHE), Tafel slope, and charge transfer resistance relative to state-of-the-art Pt/C catalyst.[80] Lower the values of these parameters, better the catalyst. We summarize these parameters of phosphorene based electrocatalysts in Table 1, which clearly suggest that phosphorene modified with functional groups, metals, and other important 2D materials show better activity. Generally, it has been found that the phosphorene composites show selective and stable H_2 production. Some of the commonly explored electrocatalysts are discussed below.

Sofer *et al.*[18] have investigated the inherent electrochemical HER activity of pristine BP electrode in an acidic medium. The edge-sites have been found to be much more active than the basal sites owing to a higher electron transfer rate at the edge sites when compared to the basal sites. The defect/edge site P atoms show higher reactivity due to the higher density of dangling bonds as well as lone pair electrons. The HER onset potentials at edge-sites and basal-sites have been found to be −0.55 V and −1.13 V,[18] respectively, which is consistent with their metallic and semiconducting nature, respectively.[81] Further, the DFT calculations have revealed that the basal plane exhibits a negligible surface energy of 9 mJ m^{-2} compared to that of the edge plane energy of 194 mJ m^{-2}.[18] Thus, one of the strategies to enhance the HER activity of phosphorene is to increase the density of defect/edge sites by making nanosheets with reduced size.[99]

Considering low ΔG_H^* values of many of the transition metal phosphides (TMPs), doping phosphorene with transition

Table 1 Electrocatalytic HER activities of phosphorene and black phosphorus based HER catalysts

Catalysts	Overpotential at 10 mA cm^{-2} *vs.* RHE	Tafel slope ($mV\ dec^{-1}$)	Electrolyte	Ref.
Pristine phosphorene	690 mV	370	0.1 M NaOH	48
Phosphorene–MoS_2	226 mV	144	0.1 M NaOH	48
Phosphorene–$MoSe_2$	330 mV	NA	0.1 M NaOH	48
BP nanosheets/MoS_2 nanoflakes	85 mV	68	0.5 M H_2SO_4	74
BP nanosheets/MoS_2 nanosheets	126 mV	68	0.5 M H_2SO_4	82
BP nanosheets/MoS_2 nanosheets	237 mV	99	1.0 M KOH	82
BP nanosheets/MoS_2 nanosheets	258 mV	154	1.0 M PBS	82
BP nanosheets/$MoSe_2$	380 mV	97	0.5 M H_2SO_4	83
BP nanosheet/N-doped graphene (1 : 4)	191 mV	76	1.0 M KOH	6
BP nanosheets/Ni_2P	185 mV	81	0.5 M H_2SO_4	84
BP nanosheets/Ni_2P	107 mV	38.6	0.5 M H_2SO_4	85
BP nanosheets/Co_2P	340 mV[a]	62	0.5 M H_2SO_4	86
BP nanosheets/Co_2P	336 mV[a]	72	1.0 M KOH	86
BP nanosheets/CoP nanodots	105 mV	92	0.5 M H_2SO_4	87
BP nanosheets/CoP nanodots	118 mV	79	1.0 M KOH	87
BP nanosheets/Pt-GR	21 mV	46.9	1.0 M KOH	88
Phosphorene quantum dots/MoS_2	600 mV	162	0.1 M KOH	89
BP nanosheet/Co_2P	305 mV	65	0.5 M H_2SO_4	90
BP nanosheet/W	500 mV	112	0.5 M H_2SO_4	90
Phosphorene/Ni	691 mV	116	0.5 M H_2SO_4	91
Phosphorene/Mo	522 mV	112	0.5 M H_2SO_4	91
Phosphorene/Co	294 mV	107	0.5 M H_2SO_4	91
Phosphorene/Cu	550 mV	139	0.5 M H_2SO_4	92
BP quantum dots/$Ti_3C_2T_X$	190 mV	83	1.0 M KOH	93
BP nanosheet/PtRu	22 mV	19	1.0 M KOH	94
BP nanosheets/Ir nanoparticles	1.98 mV	91	1.0 M KOH	95
BP nanosheets/Ir nanoparticles	25 mV	30.9	0.5 M H_2SO_4	95
BP nanosheets/Ir nanoparticles	329 mV	160	1.0 M PBS	95
Phosphorene–NH_2	290 mV	63	1.0 M KOH	51
Phosphorene/B-dopped graphene	385.9 mV	110	0.5 M H_2SO_4	96
BP nanosheets/Pd-1T–MoS_2 (in dark)	152 mV	86	0.5 M H_2SO_4	97
BP nanosheets/Pd-1T–MoS_2 (in light; >420 nm)	97 mV	66	0.5 M H_2SO_4	97
BP nanosheets/NiCoSe	206 mV	77	0.5 M H_2SO_4	98
BP nanosheets/NiCoSe	287 mV	134	1.0 M KOH	98
BP nanosheets/(NiCoSe|S)	167 mV	90	0.5 M H_2SO_4	98
BP nanosheets/(NiCoSe|S)	172 mV	128	1.0 M KOH	98

[a] Overpotential reported at 100 mA cm^{-2}; NA = not available; PBS = phosphate-buffered saline.

metals is a promising strategy for efficient H_2 evolution. To make use of higher reactivity of edge sites of phosphorene, Wang *et al.*[86] have decorated few layer BP nanosheets with dicobalt phosphide (Co_2P) from *in situ* reduction of Co^{2+} ion under an anhydrous and oxygen-free sealed reaction at high-temperatures (Fig. 5a–e). The composite exhibits low overpotential, low Tafel slope, reduced charge transfer resistance as well as enhanced ambient stability compared to bare BP nanosheets (Fig. 5f–h). Similarly, a composite of Ni_2P and BP nanosheets has been synthesized from *in situ* reduction of Ni^{2+} on the BP surface.[85] The Ni_2P particles form uniformly on the BP surface, unlike Co_2P. It is not clear from these studies that why does Ni_2P form on both edge sites and basal sites, while Co_2P form preferentially on the edge sites. A recent report has shown that under ultrahigh vacuum (UHV) conditions, initial deposition of Co metal occurs at the edge-sites of BP nanosheet, but subsequently, it deposits more on the basal-sites.[90] The Co atoms present on the edge plane transform to the $CoPO_x$ species, whilst those on the basal plane transform to $Co_2P(112)$ nanoparticles of 2–3 nm.[90] This composite shows electrocatalytic HER activity comparable to that of the edge-site functionalized Co_2P/BP composite (see Fig. 5).[86] It has been proposed that the increase in HER performance of this composite is mainly due to $Co_2P(112)$ owing to its very low ΔG_{H^*}. Liu *et al.*[91] have doped phosphorene with Co, Ni, and Mo metals by using a H-type electrochemical setup comprising platinum as the anode and a bulk BP crystal as the cathode in TBA^+Br^- (TBA = tetrabutylammonium) and metal halide electrolyte ($CoCl_2$, $NiCl_2$ or $MoCl_3$). Nafion 211 membrane has been used as a separator between the anode and the cathode. This setup enables the exfoliation of BP crystals into few-layer phosphorene by TBA^+ cation intercalation followed by deposition of metal ions on the resultant nanosheets. The metal ions then undergo *in situ* reduction to form homogeneously distributed metal nanoparticles. The HER activities follow the order, pristine BP < $BP_{(Ni)}$ < $BP_{(Mo)}$ < $BP_{(Co)}$, which is consistent with their ΔG_{H^*} trends. The ΔG_{H^*} of $BP_{(Co)}$ is close to that of thermoneutral Pt catalyst ($\Delta G_{H^*} = \sim 0$ eV). The enhancement in

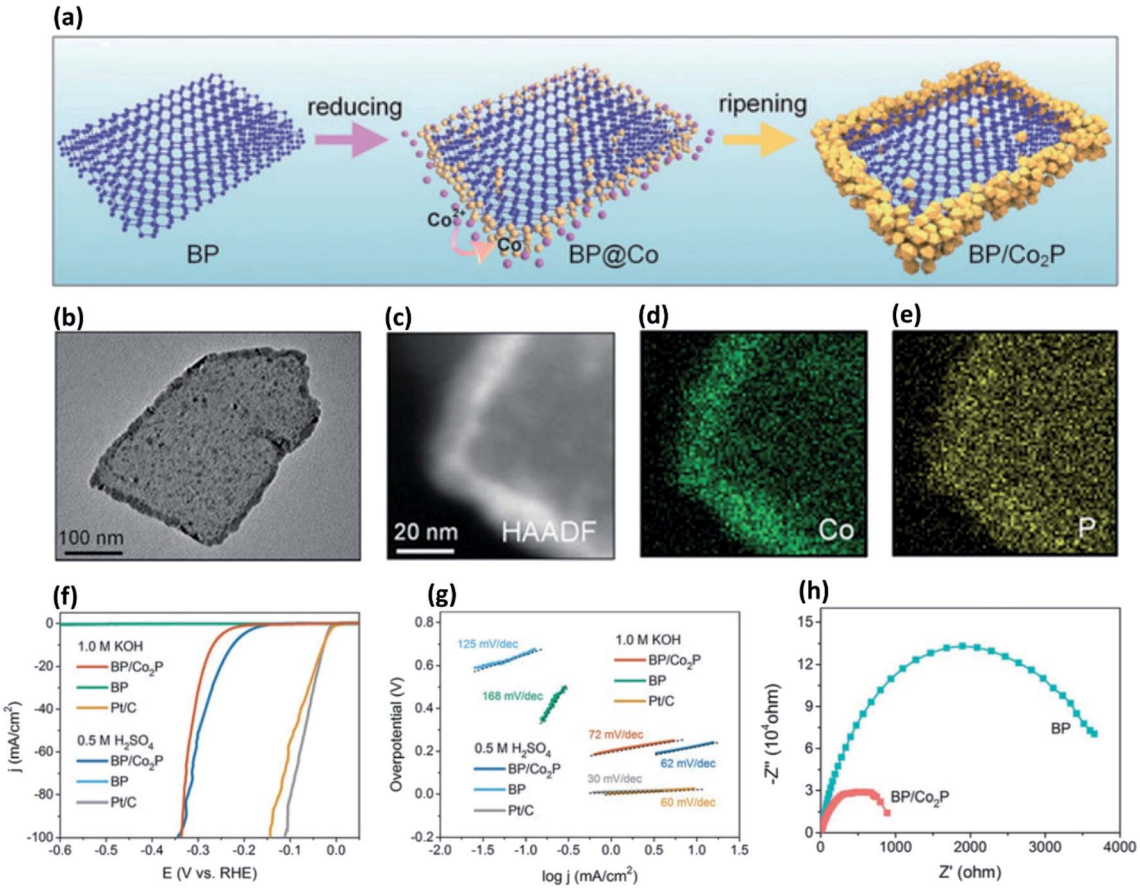

Fig. 5 (a) Schematic diagram of BP/Co_2P formation through selective interaction of Co^{2+} ions on phosphorene edge-sites and their *in situ* reduction into Co_2P. (b) Transmission electron microscope (TEM) image of a BP/Co_2P nanosheet revealing edge-sites decorated with Co_2P. (c) High-angle annular dark-field (HAADF) image of a BP/Co_2P nanosheet. (d) and (e) Corresponding energy dispersive spectroscopy (EDS) maps. (f) HER polarization curves of different catalysts in acidic and basic media. (g) Corresponding Tafel slopes. (h) Nyquist plots showing low charge-transfer resistance (R_{ct}) in the case of BP/Co_2P. The plots of pristine BP nanosheets are also given for comparison. Reproduced with permission from ref. 86, © 2018 Wiley-VCH Verlag GmbH & Co. KGaA, Weinheim.

electrocatalytic HER activity of these composites is attributed to the enhanced conductivity, optimal electronic interactions at the metal-phosphorene interface, and the stability of BP nanosheets in alkaline solution. Surprisingly, it has been demonstrated that BP activates state-of-the-art Pt catalysts through strong synergistic interaction in alkaline conditions.[88] For this purpose, a BP/Pt/graphite composite has been prepared by sonicating solvent exfoliated BP nanosheet with Pt loaded graphite. The composite forms through strong Pt–P bonds, which exhibits 6.1-fold higher HER activity than that of the Pt/C (20% Pt) catalyst. The density of states (DOS) calculations have suggested that the Pt–P bonding causes a down-shift of the Pt d-band centre, bringing more anti-bonding states below the Fermi level, giving rise to an optimal ΔG_{H^*}. Through a similar approach, PtRh nanoclusters have been immobilized on the BP nanosheet.[94] The PtRu/BP composite of $Pt_{1.0}Ru_{1.54}$ stoichiometry exhibits HER activity by an order of magnitude higher than that of the commercial Pt/C (20% Pt) catalyst in alkaline medium. Mei *et al.*[95] have prepared two different pH universal BP-Ir electrocatalysts on carbon cloth (CC) substrate; (1) BPIr_sur: by immersion of a 2 × 2 cm^2 CC piece into a dispersion of BP nanosheets and vacuum-drying followed by dipping into a dispersion of Ir nanoparticle and (2) BPIr_be: by immersion of a 2 × 2 cm^2 CC piece into a dispersion of Ir nanoparticles and vacuum-drying followed by dipping into a dispersion of BP nanosheets. In 1.0 M KOH aqueous electrolyte, BPIr_be exhibits an overpotential of only 1.98 mV at a current density of 10 mA cm^{-2}, which is superior to the BPIr_sur and BP nanosheet (105 mV, and 420 mV, respectively at a current density of 10 mA cm^{-2}) and far surpassing the Ir nanoparticles (57 mV) as well as the commercial Pt/C (76 mV) catalysts at the same current density. Even at higher current densities of 100 mA cm^{-2}, 200 mA cm^{-2}, and 400 mA cm^{-2}, BPIr_be exhibits small overpotentials of 59 mV, 87 mV, and 125 mV, respectively. The enhanced HER activity of these BPIr composites is attributed to high carrier density around the Fermi level, giving rise to higher electronic conductivity.

Although the basal plane of phosphorene is HER inactive, it provides a sufficient contact area for interfacial engineering when integrated into 2D/2D heterocomposites. 2D/2D heterocomposites are expected to show enhanced HER activity due to their large active surface area and facile interfacial charge

transfer.[100] Semiconducting 2H–MoS_2 nanosheet material is considered as a potential HER catalyst, but its inherent activity remains low due to the inertness of its basal plane.[101] However, reports have suggested that the MoS_2 basal plane can be activated by engineering interfacial charge transfer. He *et al.*[74] have deposited BP nanosheets on MoS_2 nanoflakes through van der Waals interaction. The flat-band potential of BP nanosheet (−0.29 V) is more negative than that of the MoS_2 nanosheet (-0.21 V), meaning the Fermi level of BP nanosheet lies at higher energy than that of the MoS_2 nanoflake and electrons can, therefore, flow from BP to MoS_2. Under acidic conditions, the accumulated electrons on MoS_2 effectively promote proton adsorption and reduction processes at the catalyst–electrolyte interface through Volmer [$H_{(aq)} + e^- \rightarrow H(ads)$] step as the rate-limiting step. The composite exhibits an overpotential of 85 mV at the current density of 10 mA cm^{-2}, which is superior to that of pristine BP as well as MoS_2. Another study has revealed that the HER activity of BP/MoS_2 van der Waals heterocomposite remains high, even at its large scale prepared from the hydrothermal reaction of electrochemically exfoliated BP nanosheets and $(NH_4)_2MoS_4$.[82] This composite shows electrochemical HER in all pH, but the highest activity has been observed in acidic medium, which is consistent with the electrochemical stability trends of the composite. The van der Waals heterocomposite of BP and $MoSe_2$ exhibits much lower HER activity than that of the BP and MoS_2 analogue.[83] To strengthen the interfacial charge transfer, Rao and coworkers have developed covalently cross-linked phosphorene–MoS_2 and phosphorene–$MoSe_2$ heterostructures (Fig. 6a).[48] Carboxylic acid functionalized phosphorene (P–CH_2COOH) has been coupled with primary amine functionalized MoS_2 or $MoSe_2$ (MoS_2–$CH_2CH_2NH_2$ or $MoSe_2$–$CH_2CH_2NH_2$). The P–CH_2COOH has been obtained from the reaction of phosphorene with bromoacetic acid. The MoS_2–$CH_2CH_2NH_2$ and $MoSe_2$–$CH_2CH_2NH_2$ have been obtained from the reaction of 2-bromoethylamine hydrobromide with 1T-MoS_2 and 1T-$MoSe_2$, respectively, by using a reported protocol.[102] The coupling of acid and amine groups forms interlayer amide bonds, which leads to a uniform growth of MoS_2 or $MoSe_2$ nanosheets on phosphorene nanosheets. These composites show significantly reduced overpotential, Tafel slope, and charge transfer resistance when compared to those of pristine phosphorene, MoS_2, $MoSe_2$ as well as their physical mixtures (Fig. 6b–d). We note that the long-term electrochemical stability of phosphorene–$MoSe_2$ is not as good as phosphorene–MoS_2 due to the decomposition of $MoSe_2$ under the electrochemical reaction conditions.

Compared to metal-based composite catalysts, metal-free catalysts are preferred in terms of reduced environmental effect and cost. Yuan *et al.*[6] have synthesized a metal free 2D-2D electrocatalyst with exfoliated BP (EBP) and N-doped graphene (NG) (Fig. 7a and b). The Fermi level of NG lies at a higher energy than that of EBP, which makes NG to EBP electron

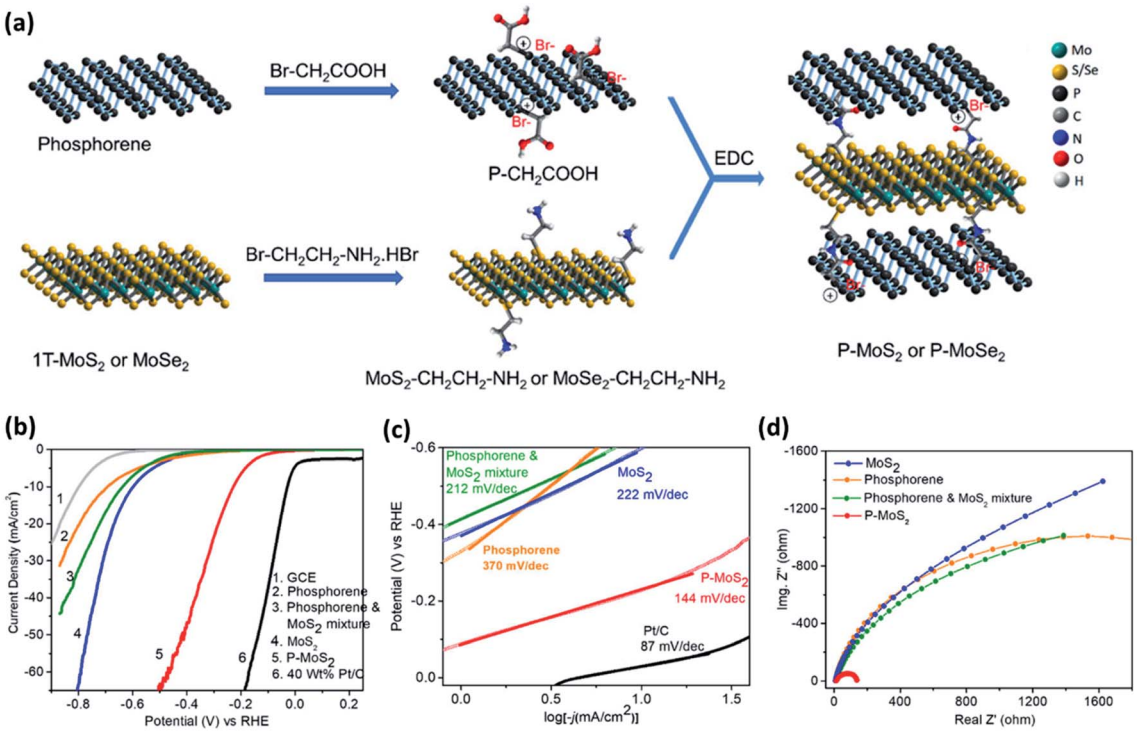

Fig. 6 (a) Schematic illustration of the preparation of covalently cross-linked phosphorene–MoS_2 and phosphorene–$MoSe_2$ heterocomposites. The amide linkages are formed by the EDC [ethyl-3-(3-dimethylaminopropyl)carbodiimide] coupling between P–CH_2COOH and MoS_2–CH_2CH_2–NH_2 or $MoSe_2$–CH_2CH_2–NH_2. (b) LSV curves of various catalysts. The curves of 40 wt% Pt/C and glassy carbon electrode (GCE) are also provided for comparison. (c) Corresponding Tafel plots revealing the lowest slope with phosphorene–MoS_2. (d) Nyquist plots showing lowest R_{ct} in the case of phosphorene–MoS_2. Reproduced with permission from ref. 48, © 2019 American Chemical Society.

transfer feasible at the heterointerface (Fig. 7c). This composite not only promotes HER on the electron enriched EBP sites, but also promotes OER on the electron depleted NG sites (Fig. 7d). Thus, the EBP@NG composite behaves as an overall water splitting catalyst, with the best performance found at the EBP to NG wt ratio of 1 : 4 (Fig. 7e and f). Shao *et al.*[51] have obtained ambient stable NH_2 functionalized BP nanosheets (NH_2-BP) of 2.15–4.87 nm thickness by ball milling BP crystals with urea. The resultant BP nanosheets exhibit abundant $-NH_2$ groups at the edges. The electrocatalytic HER in an alkaline medium indicated that NH_2-BP nanosheets need an overpotential of only 290 mV to achieve a current density of -10 mA cm^{-2}, which is ~3.1-fold less compared to the bulk BP (910 mV) and ~2.3-fold less compared to milled BP (668 mV) at the same current density. The enhanced HER activity of NH_2-BP nanosheets has been attributed to the increased density of electrochemically active surface area (ECSA) as well as feasible charge transfer due to ultra-thinness of functionalized phosphorene. These studies suggest that the density of ECSA can be controlled by morphological engineering.

Recently, it has been shown that BP nanosheets can also be utilized as overall water splitting catalysts. A heterostructure composite of nickel-cobalt sulfoselenide/BP (NiCoSe|S/BP) has been fabricated by growing NiCo hydroxide nanosheet on a few-layer BP nanosheet followed by one-step sulfoselenization.[98] The composite comprises two redox pairs: Ni^{2+}/Ni^{3+} and Co^{3+}/Co^{2+}, with the former enhancing HER through electron-donating, whilst the latter enhancing OER through electron-accepting. The composite exhibits excellent electrocatalytic performance for both HER and OER in alkaline conditions with the overpotentials of 172 mV and 285 mV, respectively at a current density of 10 mA cm^{-2}. Stable overall water splitting has been delivered at an overpotential of 1.67 V at a current density of 10 mA cm^{-2}.

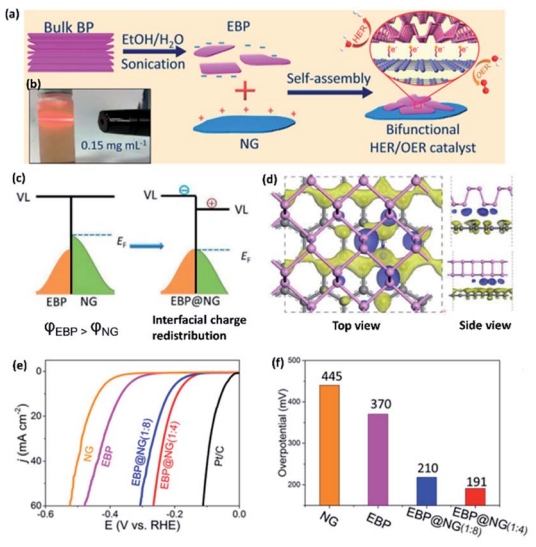

Fig. 7 (a) Schematic representation of liquid exfoliation of a BP crystal and preparation of EBP/NG composite (EBP = exfoliated BP; NG = N-doped graphene). (b) Optical image of EBP dispersion showing the Tyndall effect. (c) Illustration showing interfacial charge redistribution between EBP and NG at their Fermi levels. (d) Corresponding differential charge density map with the electron-rich and the hole-rich areas shown by blue and yellow regions, respectively. (e) LSV curves of various catalysts in 1.0 M KOH aqueous solution with the LSV curves of Pt/C and GCE are also given for comparison. (f) Corresponding bar diagram between the HER overpotentials at a current density of 10 mA cm^{-2} and the mass ratio of EBP to NG in the EBP@NG composite. Reproduced with permission from ref. 6, © 2019 American Chemical Society.

6.3. Photocatalysis

Table 2 lists the photocatalytic HER activities of phosphorene-based catalysts comprising single or composite materials. It should be noted that the HER activity depends not only on the nature of the photocatalyst but also on the experimental conditions used in the reaction. Besides, the activity numbers have been reported in a few different ways. It is, therefore, not possible to discuss an accurate comparison of efficiencies of the catalysts reported in different studies. Nevertheless, we have tabulated most of them and discussed important ones found in the commonly investigated studies.

Zhao *et al.*[103] and Zhu *et al.*[104] have reported that pristine phosphorene can promote HER under visible light irradiation (λ > 420 nm) in the presence of a sacrificial agent. Pt nanoparticles show improvement in the activity.[103] Rao and coworkers[11] have reported that the activity of pristine phosphorene can be slightly improved under the visible light illumination using eosin Y as the dye sensitizer and triethanolamine (TEOA) as the sacrificial agent. Furthermore, phosphorene has been chemically functionalized with a benzyl group, $InCl_3$, and $B(C_6F_5)_3$ (Fig. 8a). The functionalized phosphorenes exhibit several fold enhancements in the H_2 evolution rate when compared to pristine phosphorene (Fig. 8b and c). The enhanced activity has been attributed to better ambient stability, enhanced water dispersibility, and slow charge carrier recombination. Indeed, successive theoretical work has predicted that the covalent functionalization significantly reduces the ΔG_{H^*} of phosphorene close to 0.0 eV,[105] thereby facilitating hydrogen adsorption/desorption and H_2 evolution.

Generally, 2D/2D heterostructured photocatalysts show better HER activity owing to broad spectrum light absorption, large interface area, and slow charge carrier recombination.[106] In this direction, a ternary composite, Ni_2P@BP/g-C_3N_4, has been obtained by coupling Ni_2P@BP nanosheets composite with g-C_3N_4 nanosheets.[107] The composite shows charge transfer from g-C_3N_4 to Ni_2P particles through conducting BP nanosheets, exhibiting HER activity superior to the individual components. Rao and coworkers have synthesized covalently cross-linked binary heterostructures of phosphorene nanosheets with MoS_2 and $MoSe_2$ nanosheets through amide linkage (see Fig. 6a for the schematic of phosphorene–MoS_2 and phosphorene–$MoSe_2$).[48] Further, phosphorene nanosheets have been covalently cross-linked with wide bandgap 2D materials, such as BCN and g-C_3N_4, to form metal-free 2D heterocomposites.[54] These 2D heterocomposites show superior H_2 evolution rates when compared to their individual components (Fig. 8d and e). The HER activity of phosphorene–MoS_2

Table 2 Photocatalytic HER activities of phosphorene and black phosphorus based HER catalysts[a]

Catalysts	Light source	Sacrificial agent	H_2 Evolution rate	AQE (%)	Refs
Phosphorene/Pt (50 mg, 3 wt% Pt loading)	300 W Xe lamp (>420 nm)	CH_3OH	6.9 μmol h^{-1}	NA	103
Bare phosphorene (2.2 mg)	100 W halogen lamp (6 h)	TEOA	621 μmol h^{-1} g^{-1}	0.8	11
Phosphorene·$InCl_3$ (2.2 mg)	100 W halogen lamp (6 h)	TEOA	2058 μmol h^{-1} g^{-1}	2.1	11
Phosphorene·$B(C_6F_5)_3$ (2.2 mg)	100 W halogen lamp (6 h)	TEOA	6597 μmol h^{-1} g^{-1}	8.4	11
Phosphorene·CH–C_6H_5 (2.2 mg)	100 W halogen lamp (6 h)	TEOA	5691 μmol h^{-1} g^{-1}	7.3	11
Phosphorene–MoS_2 (2.5 mg)	100 W halogen lamp (6 h)	TEOA	26.8 mmol h^{-1} g^{-1}	NA	48
Phosphorene–$MoSe_2$ (2.5 mg)	100 W halogen lamp (6 h)	TEOA	20.7 mmol h^{-1} g^{-1}	NA	48
Phosphorene–BCN	100 W halogen lamp (6 h)	TEOA	6528 μmol h^{-1} g^{-1}	NA	54
Phosphorene–*g*-C_3N_4	100 W halogen lamp (6 h)	TEOA	11 274 μmol h^{-1} g^{-1}	NA	54
BP nanosheet/MoS_2 (10 mg)	300 W Xenon lamp (≥420 nm)	Na_2S/Na_2SO_3	1286 μmol h^{-1} g^{-1}	1.2	114
BP nanoflakes/*g*-C_3N_4 nanosheet (1 : 4) (1.5 mg)	320 W Xenon lamp (≥420 nm)	Methanol	427 μmol h^{-1} g^{-1}	3.18	108
BP nanoflakes/*g*-C_3N_4 nanosheet (1 : 4) (1.5 mg)	320 W Xenon lamp (≥780 nm)	Methanol	101 μmol h^{-1} g^{-1}	1.1	108
Phosphorene/*g*-C_3N_4 nanosheet (20 mg)	300 W Xenon lamp (≥420 nm)	LA	571 μmol h^{-1} g^{-1}	1.2	109
BPQDs-*g*-C_3N_4 (100 mg)	200 W Xenon lamp	Methanol	190 μmol h^{-1}	NA	115
BP nanosheet/*g*-C_3N_4 (10 mg)	300 W Xenon (≥420 nm) (24 h)	TEOA	384.17 μmol g^{-1} h^{-1}	NA	110
Phosphorene/CdS (20 mg)	300 W Xenon (≥420 nm) (4 h)	LA	11 192 μmol h^{-1} g^{-1}	34.7	112
BPQDs/Au nanorod/CdS nanowire (20 mg)	300 mW cm^{-2} Xe lamp	Na_2S/Na_2SO_3	10.1 mmol h^{-1} g^{-1}	2.3	116
BP nanosheets/Co_2P (40 mg)	300 W Xe lamp (≥420 nm)	w/o sacrificial	29.4 μmol h^{-1}	42.55	117
BP nanosheet/$BiVO_4$ (5 mg)	320 W Xe lamp (≥420 nm) (3 h)	w/o sacrificial	0.80 μmol	0.89	118
BP nanosheet/$BiVO_4$/Co_3O_4 (5 mg)	320 W Xe lamp (≥420 nm) (3 h)	w/o sacrificial	3.9 μmol	NA	118
BP nanosheet/$BiVO_4$/Co_3O_4 (5 mg)	320 W Xe lamp (≥420 nm) (3 h)	EDTA	7.5 μmol	NA	118
BP nanosheet/Bi_2WO_6 (20 mg, 3 wt% $H_2PtCl_6·6H_2O$ loading)	300 W Xe lamp	TEOA	21042 μmol g^{-1}	NA	119
BP-MoS_2/CdS (1.0 mg)	150 W Xe (5 h)	LA	183.24 mmol g^{-1} h^{-1}	63.1	120
BP/Pt/RGO (BP, 0.2 mg; Pt, 75 μg; RGO, 0.1 mg)	320 W Xe lamp (4 h)	EDTA	3.4 mmol g^{-1} h^{-1} (>420 nm)	8.7	121
			0.84 mmol g^{-1} h^{-1} (>780 nm)	1.5	
BP-Au/$La_2Ti_2O_7$ (1.5 mg)	320 W Xe lamp (3 h)	Methanol	0.74 mmol g^{-1} h^{-1} (>420 nm)	NA	122
			0.30 mmol g^{-1} h^{-1} (>780 nm)	NA	
			1.49 mmol g^{-1} h^{-1} (UV-Vis-NIR)	NA	
BP QDs-CdS-$La_2Ti_2O_7$ (20 mg)	300 mW cm^{-2} Xe lamp	Na_2S/Na_2SO_3	0.96 mmol g^{-1} h^{-1} (UV-Vis-NIR)	NA	123
			0.80 mmol g^{-1} h^{-1} (≥420 nm)	NA	
			0.26 mmol g^{-1} h^{-1} (≥700 nm)	NA	
Ni_2P@BP/C_3N_4 (20 mg)	300 W Xe lamp (≥420 nm) (5 h)	TEOA	858.2 μmol g^{-1} h^{-1}	2.8	107
BP/TiO_2 (25 mg)	300 W Xe lamp (365 nm) (6 h)	TEOA	122.27 μmol	18.23	124
$Zn_xCd_{1-x}S$/few-layer phosphorene (20 mg)	300 W Xe lamp (≥420 nm)	LA	9326 μmol h^{-1} g^{-1}	21.5	113
BP/WS_2 (0.2 mL dispersion)	100 mW cm^{-2} simulated solar (3 h)	EDTA	9.61 μmol	NA	125
BP/WS_2 (0.2 mL dispersion)	320 W Xe lamp (3 h)	EDTA	1.55 μmol (≥808 nm)	NA	125
			2.49 μmol (≥780 nm)	2.06	
BP/*g*-C_3N_4-HKUST-1 (20 mg)	300 W Xe lamp (≥400 nm)	TEOA	7380 μmol h^{-1} g^{-1}	NA	126
0.5%Pt/0.5%BP/$ZnIn_2S_4$ (20 mg)	300 W Xe lamp (≥420 nm)	Na_2SO_3/Na_2S	1278 μmol h^{-1} g^{-1}	0.25	127
BP/Ti_3C_2/*g*-C_3N_4 (10 mg; 2 wt% Pt loading)	300 W Xe lamp (≥420 nm)	TEOA	18.42 mmol h^{-1} g^{-1}	17.6	111
m-*g*-CN/BP	Solar simulator 300 W (≥420 nm)	TEOA	330 μmol g^{-1} h^{-1}	NA	128
m-*g*-CN/BP-Ni	Solar simulator 300 W (≥420 nm)	TEOA	442 μmol h^{-1} g^{-1}	NA	128
m-*g*-CN/BP-Co	Solar simulator 300 W (≥420 nm)	TEOA	326 μmol h^{-1} g^{-1}	NA	128
m-*g*-CN/BP-Cu	Solar simulator 300 W (≥420 nm)	TEOA	223 μmol h^{-1} g^{-1}	NA	128
CdS-BP/Co (20 mg)	300 W Xe lamp (≥420 nm)	LA	345.4 μmol h^{-1}	NA	129
Pt-BP/CdS (20 mg)	300 W Xe lamp (≥420 nm)	LA	24.17 mmol h^{-1} g^{-1}	46.0	130

[a] TEOA = triethanolamine; LA = lactic acid; EDTA = ethylenediaminetetraacetic acid; AQE = apparent quantum efficiency; NA = not available.

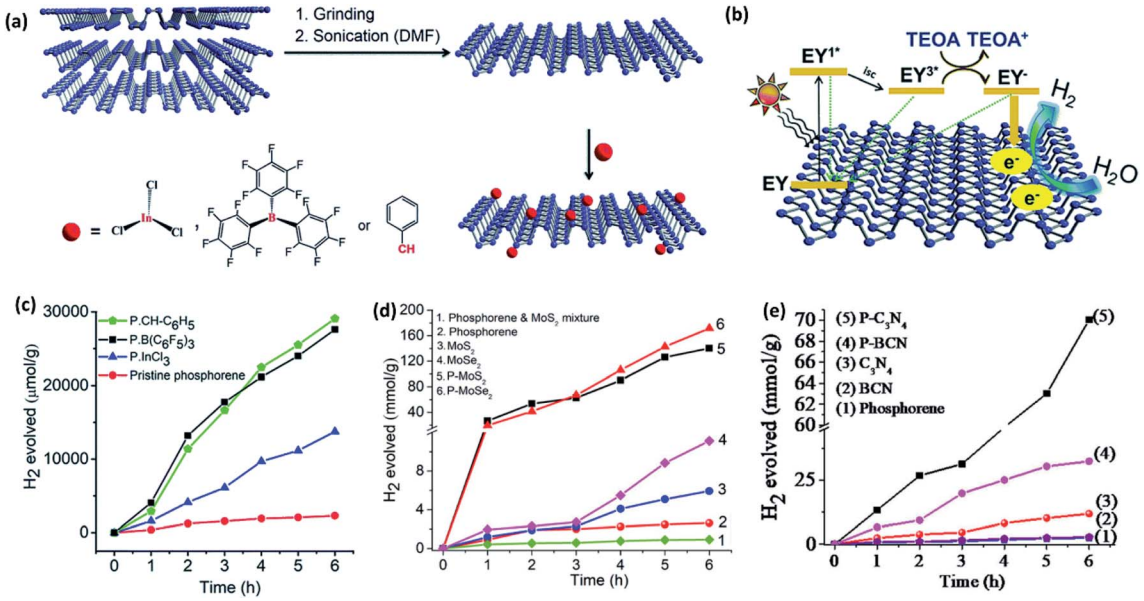

Fig. 8 (a) Schematic representation of liquid exfoliation of BP into phosphorene nanosheets and their functionalization with $InCl_3$, $B(C_6F_5)_3$ and benzyl group. (b) Plausible mechanism of eosin Y sensitised photocatalytic HER in the presence of TEOA as a sacrificial agent. (c) Hydrogen evolved *versus* time plots of pristine and functionalized phosphorenes. (d) Hydrogen evolved *versus* time plots of covalently cross-linked phosphorene–MoS_2 and phosphorene–$MoSe_2$ composites. (e) Hydrogen evolved *versus* time plots of metal-free covalently cross-linked phosphorene–C_3N_4 and phosphorene–BCN composites. Panels (a–c) reproduced with permission from ref. 11, © 2019. The Royal Society of Chemistry. Panel (d) reproduced with permission from ref. 48, © 2019 American Chemical Society. Panel (e) reproduced with permission from ref. 54, ©Author(s) 2020.

composite is as high as 26.8 mmol h^{-1} g^{-1}, which is ~30-fold enhanced compared to pristine phosphorene and ~22-fold compared to few layer MoS_2 under similar reaction conditions. The activity of phosphorene–MoS_2 is also superior to many other catalysts (Table 2). Similar HER activity trends have been found in the case of phosphorene–$MoSe_2$, phosphorene–BCN, and phosphorene–*g*-C_3N_4 composites, but their activities are lower compared to the phosphorene–MoS_2 composite.

Zhu *et al.*[108] have synthesized a metal-free 2D/2D heterocomposite of phosphorene with *g*-C_3N_4 in different stoichiometries (Fig. 9a). The 1 : 4 composite shows the highest H_2 evolution rate of 427 μmol g^{-1} h^{-1} for several days, while pristine phosphorene and *g*-C_3N_4 have shown negligible H_2 evolution under similar reaction conditions (Fig. 9b and c). The composite forms a type-I heterojunction in which the photoexcited electrons transfer from *g*-C_3N_4 to phosphorene, where they are consumed in the proton reduction into H_2. The directional electron transfer has been further strengthened by P–N bonds between the exposed P and N atoms on the phosphorene and the *g*-C_3N_4 surfaces, respectively. It has been proposed that P–N interactions introduce shallow charge trapping sites, which slow down the charge carrier recombination. Similar trends have been witnessed in a type-I phosphorene/*g*-C_3N_4 van der Waals heterostructure (Fig. 9d), exhibiting even higher HER activity than that of Pt loaded *g*-C_3N_4 (Fig. 9e).[109] The photoexcited electrons migrate from *g*-C_3N_4 to phosphorene, creating electron accumulated sites on phosphorene and electron depleted sites on g-C_3N_4 (Fig. 9f). Another study has revealed that the combination of phosphorene (bandgap of 1.39 eV) and *g*-C_3N_4 (bandgap of 2.70 eV) leads to enhanced H_2 evolution under broad-spectrum light irradiation.[110] The composite exhibits much higher activity under the light of wavelength >420 nm when compared to >475 nm. *g*-C_3N_4, being a wide bandgap material, cannot be excited with the light of wavelength >475 nm and the catalysis occurs only on the phosphorene component. A conducting MXene (Ti_3C_2) layer between phosphorene quantum dots and the *g*-C_3N_4 layer enhances the interfacial charge transfer.[111] The combination of phosphorene quantum dots and *g*-C_3N_4 improves visible light capture, and the MXene nanosheets mediate the migration of photoexcited charge carriers to the catalyst surface.

Compared to type-I heterojunction, type-II heterojunction is expected to provide much more efficient charge separation.[106] Ran *et al.*[112] have shown that a type-II heterostructure (Fig. 9g and h) of phosphorene nanosheets (4–5 nm thickness) with cadmium sulphide nanoparticles (10–60 nm diameter) exhibits a superior H_2 production rate of 11 192 μmol h^{-1} g^{-1} (Fig. 9i). It is noteworthy that the HER activity reduces due to the formation of type-I heterojunction when the thickness of phosphorene nanosheets is increased to 8–11 nm or beyond. Similar type-II band alignment and HER trends have been observed in the case of $Zn_xCd_{1-x}S$ nanoparticles (*ca.* 15–60 nm diameter) loaded on phosphorene nanosheets of 5–6 nm thickness.[113]

Most of the above photocatalytic studies have shown the utility of the photoexcited electrons in H_2 evolution at the CBM, whilst the photogenerated holes at the VBM are quenched by using sacrificial agents. Zhu *et al.*[118] have prepared a 2D/2D

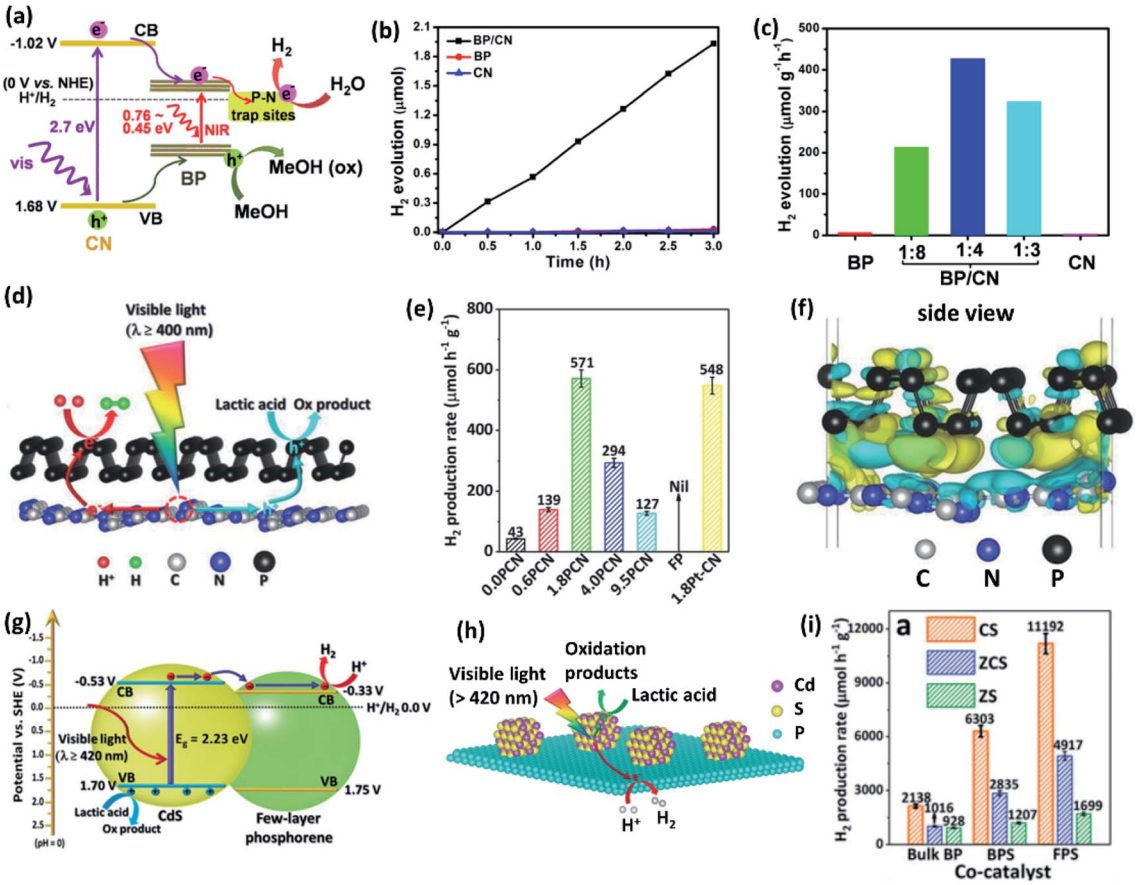

Fig. 9 (a) Schematic diagram of visible light photocatalytic HER mechanism of BP/CN composite in the presence of methanol (20 vol%). (b) Corresponding HER activity *versus* time plots for different catalysts. (c) Effect of BP : CN weight ratio on HER activity under visible light irradiation for 3 h. (d) Schematic of visible light H_2 production by the phosphorene/g-C_3N_4 catalysts in 18 vol% lactic acid aqueous solution. (e) HER activities of phosphorene/g-C_3N_4 with 0.0, 0.6, 1.8, 4.0 and 9.5 wt% of phosphorene. (f) Differential charge density map of phosphorene/g-C_3N_4 with the iso-surface value of 0.00015 e Å^{-3} with the electron accumulation and depletion areas are represented by yellow and blue regions, respectively. (g) and (h) Illustration of type-II band alignment and photocatalytic HER mechanism of few-layer phosphorene/CdS (FPS/CS) composite. (i) Comparison of photocatalytic HER activities of 1.0 wt% bulk BP, BPS (8–11 nm thick BP nanosheet) or FPS (4–5 nm thick BP nanosheet) composites with CdS (CS), $Zn_{0.8}Cd_{0.2}S$ (ZCS) and ZnS (ZS). Panels (a–c) reproduced with permission from ref. 108, © 2017 American Chemical Society. Panels (d–f) reproduced with permission from ref. 109, © 2018 Wiley-VCH Verlag GmbH & Co. KGaA, Weinheim. Panels (g–i) reproduced with permission from ref. 112, © 2017 Wiley-VCH Verlag GmbH & Co. KGaA, Weinheim.

heterostructure of BP (0.2 μm–2.0 μm) and monoclinic bismuth vanadate ($BiVO_4$) (0.1 μm–1.0 μm) nanosheets through electrostatic interaction. The BP/$BiVO_4$ composite catalyzes the overall water splitting reaction through an artificial Z-scheme photocatalytic system (Fig. 10a). The monoclinic $BiVO_4$ is a narrow bandgap (2.4–2.5 eV) layered semiconductor, which has the ability to promote OER. On visible light irradiation, the photogenerated electrons in the CBM of $BiVO_4$ quickly recombine with the photogenerated holes in the VBM of BP owing to their close energies and staggered alignment. In this way, the electrons are utilized in the HER at the CBM of BP, whilst the holes are utilized in the OER at the VBM of $BiVO_4$. The composite shows superior H_2 and O_2 production rates under visible light irradiation, even in the absence of a sacrificial agent and co-catalyst (Fig. 10b). The HER activity further increases with the assistance of Co_3O_4 as co-catalyst and EDTA as a sacrificial agent. The optimum HER and OER activities have been observed with 20 wt% BP in the composite, while stoichiometric H_2 and O_2 evolution has been detected with 40 wt% BP. Similarly, BP nanosheets and monolayer Bi_2WO_6 have been combined in a Z-scheme photocatalyst, exhibiting HER activity superior to the BP/$BiVO_4$ composite owing to broad spectrum light absorption.[119]

6.4. Photo-electrocatalysis (PEC)

Of late, there has been an increase of interest in PEC, which is the combination of photocatalysis and electrocatalysis techniques. Typically, in this method, the HER is carried out with applied potential on a photoelectrode supported by a semiconductor catalyst. It allows more effective separation of photogenerated electron–hole, charge transfer, and enhanced light absorption, thereby increasing the overall energy efficiency of water splitting. Under light irradiation, TiO_2 nanorods coated with BP nanosheets show a 140% increase in the incident-photo-current conversion efficiency (IPCE).[131] Similarly,

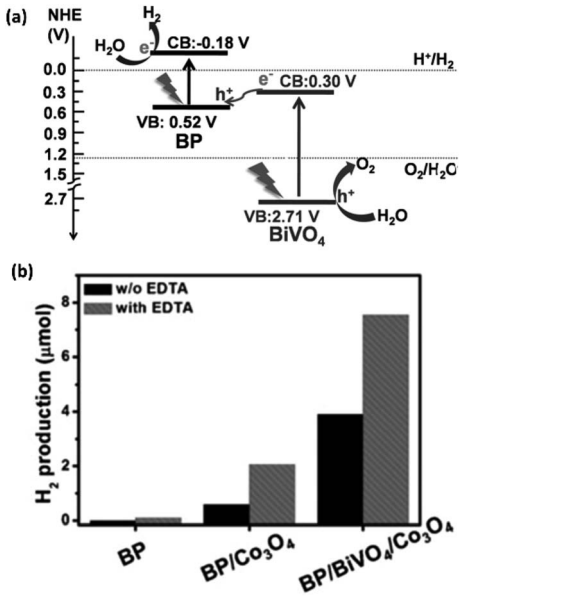

Fig. 10 (a) Schematic presentation of BP/$BiVO_4$ composite based Z-scheme photocatalyst for visible and NIR radiation (>420 nm) induced overall water splitting. (b) H_2 evolved by different catalysts with and without Co_3O_4 co-catalyst and EDTA sacrificial agent under >420 nm light irradiation. Reproduced with permission from ref. 118, © 2018 Wiley-VCH Verlag GmbH & Co. KGaA, Weinheim.

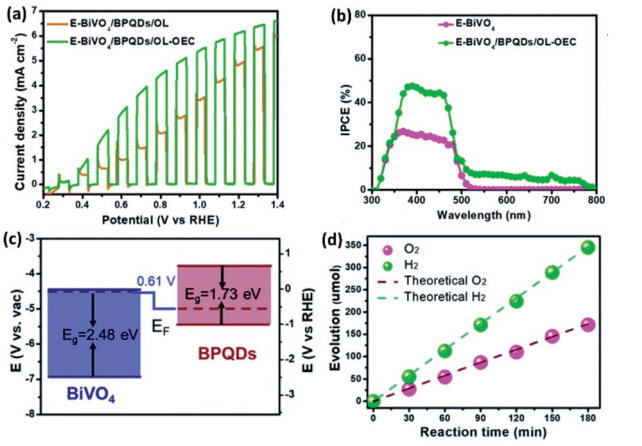

Fig. 11 (a) *J–V* curves of E-$BiVO_4$/BPQDs/OL and E-$BiVO_4$/BPQDs/OL-OEC. (b) IPCE values of E-$BiVO_4$ and E-$BiVO_4$/BPQDs/OL-OEC. (c) Band alignment diagram of E-$BiVO_4$ and BPQDs showing type II heterojunction. (d) HER and OER activities of the E-$BiVO_4$/BPQDs/OL-OEC photoanode at 1.23 V *vs.* RHE. Reproduced with permission from ref. 133 © 2022 The Royal Society of Chemistry.

enhancement of photocurrent densities of BP/Pt/RGO nanoflakes electrode has been observed under >420 nm or >808 nm light irradiation when compared to dark.[121] Recently, it has been reported that van der Waals heterostructure of Pd dopped 1T-MoS_2 and BP nanosheet exhibits increased light absorption when compared to Pd-1T-MoS_2.[97] Under the light irradiation, the composite shows a decrease in the overpotential from 152 mV to 97 mV at the current density of 10 mA cm^{-2} with a concomitant decrease in the Tafel slope from 86 mV dec^{-1} to 66 mV dec^{-1}.

Furthermore, BP quantum dots (BPQDs) have the capability of harvesting the full visible light spectrum due to size-dependent bandgaps.[67,132] The composite of BPQD and *g*-C_3N_4 nanosheets has been shown to exhibit enhanced photocatalytic HER activity as well as photocurrent when irradiated with 420 nm laser light.[115] The optimal photocurrent of 9.11 μA cm^{-2} has been obtained on 7 wt% loading of BPQD on *g*-C_3N_4 nanosheets. To utilize the broad light absorption capability of BPQDs, Jin *et al.*[133] have fabricated a two-photon E-$BiVO_4$/BPQDs/OL-OEC (E-$BiVO_4$ = etched $BiVO_4$) photoanode passivated with TiO_2 overlayer (OL) and coated with NiOOH as oxygen evolution catalyst (OEC). The anode shows a remarkable photocurrent density of 6.2 mA cm^{-2} at 1.23 V *vs.* RHE, under AM 1.5 illumination (Fig. 11a). The BPQDs not only enhance the incident photon-to-electron conversion efficiencies (IPCEs), but also extends the light harvesting window up to 800 nm (Fig. 11b). The TiO_2 overlayer enhances the ambient stability of BPQD and eliminates the surface trap state. The type-II band alignment (Fig. 11c) of BPQDs and E-$BiVO_4$ promotes efficient separation of charge carriers. NiOOH enhances sluggish O_2 evolution kinetics and consequently the E-$BiVO_4$/BPQDs/OL-OEC photoanode exhibits H_2 and O_2 evolution ~2 : 1 molar ratio for over 180 min at a photocurrent density of 6.2 mA cm^{-2} at 1.23 V *vs.* RHE (Fig. 11d).

7. Conclusions and future opportunities

We have discussed a range of phosphorenes modified with functional groups, atoms/ions, and other catalytically important 2D materials. We have summarized key methods of stabilizing phosphorenes by chemical functionalization as well as interfacial engineering. With appropriate examples, we have discussed diverse interactions (covalent, coordination, electrostatic, van der Waals, charge-transfer, and interfacial) which have been utilized in the functionalization of phosphorene. Although covalent functionalization is an effective approach to functionalize and generate different materials with improved properties, sometimes it leads to a low degree of functionalization as well as P–P bond breaking, affecting the properties of phosphorene. The non-covalent functionalization protects phosphorene with little (or no) distortion of the lattice, provides a relatively higher degree of functionalization, and enhances electronic properties.

We have highlighted that phosphorene composites are superior catalysts for H_2 production from water splitting reaction and have the potential to replace state-of-the-art Pt metal and Pt group metals. In addition, it is comprised of phosphorus, which is an earth abundant and non-toxic element. However, large-scale practical applications of phosphorene are still limited primarily due to ambient instability and lack of scalable synthesis. We expect that the interest in the chemistry and the applications of phosphorene continue to surge and develop along the following lines:

(1) Understanding chemistry: despite plenty of experimental reports on the stabilization of phosphorene, the long-term stability in oxygen and water is yet to be explored. Further understanding of the chemistry of degradation[134] as well as passivation of phosphorene is thus necessary. Quantification of the degree of functionalization remains still a challenge.[135] Thus, advanced tools need to be developed to elucidate the degree of functionalization and quality control so that the electronic properties can be appropriately optimized for efficient catalysis and other applications. For example, fluorescence labelling of surface species (FLOSS) can potentially be used as an *in situ* method.[136]

(2) Large scale synthesis: although liquid exfoliation has become a significant method of phosphorene synthesis, it has limitations, including uncontrollable lateral size, layer thickness and morphology, solvent contamination, oxidation of sample and formation of structural defects, all of which affect the overall performance. Bottom-up synthetic strategies such as pulsed laser deposition (PLD) have a great potential for high-quality scalable synthesis.[137] There is a scope to further developing the top-down approaches such as electrochemical and shear exfoliation.

(3) Metal-free catalysis: *p*-block elements have the potential to replace the rare and precious noble and other transition metals-based catalysts. Superior HER activities of phosphorene/BCN and phosphorene/N-doped graphene suggest that phosphorene could potentially be used as a metal-free catalyst at a commercial scale. However, the developments of metal-free heterosystems are still at an early stage, and there is considerable scope for future developments. For example, phosphorene–borocarbonitride (B*x*C*y*N*z*) composite is worth exploring where electronic properties can be tuned by varying composition of the latter.

After possible developments of efficient HER catalysts, the realization of the potential of water as a completely renewable hydrogen source could be a viable solution. Solar water splitting reactors need to be developed to ensure large scale production at a low cost. In this direction, the reactors based on photoelectrochemical (PEC) cells have the advantage of using solar as well as electrical energy and simultaneously separating evolved H_2 from O_2. Bandgap tuneable and high conductivity make phosphorene a promising PEC material for high solar-to-hydrogen efficiency. Besides, strategies for hydrogen storage and transport need to be developed.

Conflicts of interest

There are no conflicts to declare.

Acknowledgements

PV acknowledges the Science & Engineering Research Board (SERB) of the Govt. of India for Ramanujan Fellowship (Award No. RJF/2020/000106) and the Jawaharlal Nehru Centre for Advanced Scientific Research (JNCASR) Bangalore for financial support and research infrastructure.

Notes and references

1 C. N. R. Rao and S. Dey, *Proc. Natl. Acad. Sci.*, 2017, **114**, 13385–13393.
2 J. Zhu, L. Hu, P. Zhao, L. Y. S. Lee and K.-Y. Wong, *Chem. Rev.*, 2020, **120**, 851–918.
3 M. Chhetri, S. Maitra, H. Chakraborty, U. V. Waghmare and C. N. R. Rao, *Energy Environ. Sci.*, 2016, **9**, 95–101.
4 Y. Zheng, Y. Jiao, Y. Zhu, L. H. Li, Y. Han, Y. Chen, A. Du, M. Jaroniec and S. Z. Qiao, *Nat. Commun.*, 2014, **5**, 3783.
5 M. Latorre-Sánchez, A. Primo and H. García, *Angew. Chem., Int. Ed.*, 2013, **52**, 11813–11816.
6 Z. Yuan, J. Li, M. Yang, Z. Fang, J. Jian, D. Yu, X. Chen and L. Dai, *J. Am. Chem. Soc.*, 2019, **141**, 4972–4979.
7 H. Liu, A. T. Neal, Z. Zhu, Z. Luo, X. Xu, D. Tománek and P. D. Ye, *ACS Nano*, 2014, **8**, 4033–4041.
8 L. Li, Y. Yu, G. J. Ye, Q. Ge, X. Ou, H. Wu, D. Feng, X. H. Chen and Y. Zhang, *Nat. Nanotechnol.*, 2014, **9**, 372–377.
9 Y. Deng, Z. Luo, N. J. Conrad, H. Liu, Y. Gong, S. Najmaei, P. M. Ajayan, J. Lou, X. Xu and P. D. Ye, *ACS Nano*, 2014, **8**, 8292–8299.
10 A. N. Abbas, B. Liu, L. Chen, Y. Ma, S. Cong, N. Aroonyadet, M. Köpf, T. Nilges and C. Zhou, *ACS Nano*, 2015, **9**, 5618–5624.
11 P. Vishnoi, U. Gupta, R. Pandey and C. N. R. Rao, *J. Mater. Chem. A*, 2019, **7**, 6631–6637.
12 M. Z. Rahman, C. W. Kwong, K. Davey and S. Z. Qiao, *Energy Environ. Sci.*, 2016, **9**, 709–728.
13 B. Sa, Y.-L. Li, J. Qi, R. Ahuja and Z. Sun, *J. Phys. Chem.*, 2014, **118**, 26560–26568.
14 Y. Cai, J. Gao, S. Chen, Q. Ke, G. Zhang and Y.-W. Zhang, *Chem. Mater.*, 2019, **31**, 8948–8956.
15 J. Li, P. Liu, H. Huang, Y. Li, Y. Tang, D. Mei and C. Zhong, *ACS Sustain. Chem. Eng.*, 2020, **8**, 5175–5183.
16 X. Zhu, S. Huang, Q. Yu, Y. She, J. Yang, G. Zhou, Q. Li, X. She, J. Deng, H. Li and H. Xu, *Appl. Catal. B Environ.*, 2020, **269**, 118760.
17 G.-Q. Zhao, J. Hu, X. Long, J. Zou, J.-G. Yu and F.-P. Jiao, *Small*, 2021, **17**, 2102155.
18 Z. Sofer, D. Sedmidubský, Š. Huber, J. Luxa, D. Bouša, C. Boothroyd and M. Pumera, *Angew. Chem., Int. Ed.*, 2016, **55**, 3382–3386.
19 S. Li, Y. Zhang and H. Huang, *J. Energy Chem.*, 2022, **67**, 745–779.
20 Z. Wu, J. Qi, W. Wang, Z. Zeng and Q. He, *J. Mater. Chem. A*, 2021, **9**, 18793–18817.
21 A. M. Kuchkaev, S. Lavate, A. M. Kuchkaev, A. V. Sukhov, R. Srivastava and D. G. Yakhvarov, *Energy Technol.*, 2021, **9**, 2100581.
22 P. W. Bridgman, *J. Am. Chem. Soc.*, 1914, **36**, 1344–1363.
23 J. C. Jamieson, *Science*, 1963, **139**, 1291–1292.
24 Y. Akahama, S. Endo and S. Narita, *J. Phys. Soc. Jpn.*, 1983, **52**, 2148–2155.
25 J. Wittig and B. T. Matthias, *Science*, 1968, **160**, 994–995.
26 K. S. Novoselov, A. K. Geim, S. V. Morozov, D. Jiang, Y. Zhang, S. V. Dubonos, I. V. Grigorieva and A. A. Firsov, *Science*, 2004, **306**, 666–669.

27 D. Scelta, A. Baldassarre, M. Serrano-Ruiz, K. Dziubek, A. B. Cairns, M. Peruzzini, R. Bini and M. Ceppatelli, *Angew. Chem., Int. Ed.*, 2017, **56**, 14135–14140.
28 X. Li, J. Sun, P. Shahi, M. Gao, A. H. MacDonald, Y. Uwatoko, T. Xiang, J. B. Goodenough, J. Cheng and J. Zhou, *Proc. Natl. Acad. Sci.*, 2018, **115**, 9935–9940.
29 Y. Akahama, M. Miyakawa, T. Taniguchi, A. Sano-Furukawa, S. Machida and T. Hattori, *J. Chem. Phys.*, 2020, **153**, 14704.
30 P. Vishnoi, K. Pramoda and C. N. R. Rao, *ChemNanoMat*, 2019, **5**, 1062–1091.
31 J. Qiao, X. Kong, Z.-X. Hu, F. Yang and W. Ji, *Nat. Commun.*, 2014, **5**, 4475.
32 X. Wang, A. M. Jones, K. L. Seyler, V. Tran, Y. Jia, H. Zhao, H. Wang, L. Yang, X. Xu and F. Xia, *Nat. Nanotechnol.*, 2015, **10**, 517–521.
33 R. Fei, A. Faghaninia, R. Soklaski, J.-A. Yan, C. Lo and L. Yang, *Nano Lett.*, 2014, **14**, 6393–6399.
34 P. Yasaei, B. Kumar, T. Foroozan, C. Wang, M. Asadi, D. Tuschel, J. E. Indacochea, R. F. Klie and A. Salehi-Khojin, *Adv. Mater.*, 2015, **27**, 1887–1892.
35 A. Ambrosi, Z. Sofer and M. Pumera, *Angew. Chem., Int. Ed.*, 2017, **56**, 10443–10445.
36 J. Yang, R. Xu, J. Pei, Y. W. Myint, F. Wang, Z. Wang, S. Zhang, Z. Yu and Y. Lu, *Light: Sci. Appl.*, 2015, **4**, e312.
37 T. Low, A. S. Rodin, A. Carvalho, Y. Jiang, H. Wang, F. Xia and A. H. Castro Neto, *Phys. Rev. B*, 2014, **90**, 075434.
38 C. N. R. Rao, U. Maitra and U. V. Waghmare, *Chem. Phys. Lett.*, 2014, **609**, 172–183.
39 W. Hu, L. Lin, R. Zhang, C. Yang and J. Yang, *J. Am. Chem. Soc.*, 2017, **139**, 15429–15436.
40 G. Abellán, S. Wild, V. Lloret, N. Scheuschner, R. Gillen, U. Mundloch, J. Maultzsch, M. Varela, F. Hauke and A. Hirsch, *J. Am. Chem. Soc.*, 2017, **139**, 10432–10440.
41 Y. Huang, J. Qiao, K. He, S. Bliznakov, E. Sutter, X. Chen, D. Luo, F. Meng, D. Su, J. Decker, W. Ji, R. S. Ruoff and P. Sutter, *Chem. Mater.*, 2016, **28**, 8330–8339.
42 J. D. Wood, S. A. Wells, D. Jariwala, K.-S. Chen, E. Cho, V. K. Sangwan, X. Liu, L. J. Lauhon, T. J. Marks and M. C. Hersam, *Nano Lett.*, 2014, **14**, 6964–6970.
43 T. Zhang, Y. Wan, H. Xie, Y. Mu, P. Du, D. Wang, X. Wu, H. Ji and L. Wan, *J. Am. Chem. Soc.*, 2018, **140**, 7561–7567.
44 A. Favron, E. Gaufrès, F. Fossard, A.-L. Phaneuf-ĹHeureux, N. Y. W. Tang, P. L. Lévesque, A. Loiseau, R. Leonelli, S. Francoeur and R. Martel, *Nat. Mater.*, 2015, **14**, 826–832.
45 Q. Zhou, Q. Chen, Y. Tong and J. Wang, *Angew. Chem., Int. Ed.*, 2016, **55**, 11437–11441.
46 C. R. Ryder, J. D. Wood, S. A. Wells, Y. Yang, D. Jariwala, T. J. Marks, G. C. Schatz and M. C. Hersam, *Nat. Chem.*, 2016, **8**, 597–602.
47 S. Yasui, M. Fujii, C. Kawano, Y. Nishimura, K. Shioji and A. Ohno, *J. Chem. Soc., Perkin Trans.*, 1994, **2**, 177–183.
48 P. Vishnoi, K. Pramoda, U. Gupta, M. Chhetri, R. G. Balakrishna and C. N. R. Rao, *ACS Appl. Mater. Interfaces*, 2019, **11**, 27780–27787.
49 Y. Liu, P. Gao, T. Zhang, X. Zhu, M. Zhang, M. Chen, P. Du, G.-W. Wang, H. Ji, J. Yang and S. Yang, *Angew. Chem., Int. Ed.*, 2019, **58**, 1479–1483.
50 K. L. Walz Mitra, C. H. Chang, M. P. Hanrahan, J. Yang, D. Tofan, W. M. Holden, N. Govind, G. T. Seidler, A. J. Rossini and A. Velian, *Angew. Chem., Int. Ed.*, 2021, **60**, 9127–9134.
51 L. Shao, H. Sun, L. Miao, X. Chen, M. Han, J. Sun, S. Liu, L. Li, F. Cheng and J. Chen, *J. Mater. Chem. A*, 2018, **6**, 2494–2499.
52 Z. Sofer, J. Luxa, D. Bouša, D. Sedmidubský, P. Lazar, T. Hartman, H. Hardtdegen and M. Pumera, *Angew. Chem., Int. Ed.*, 2017, **56**, 9891–9896.
53 J. Zhang, S. Chen, Y. Ma, D. Wang, J. Zhang, Y. Wang, W. Li, Z. Yu, H. Zhang, F. Yin and Z. Li, *J. Mater. Chem. B*, 2018, **6**, 4065–4070.
54 C. N. R. Rao, K. Pramoda, A. Saraswat, R. Singh, P. Vishnoi, N. Sagar and A. Hezam, *APL Mater.*, 2020, **8**, 20902.
55 M. Trunk, J. F. Teichert and A. Thomas, *J. Am. Chem. Soc.*, 2017, **139**, 3615–3618.
56 A. Ienco, G. Manca, M. Peruzzini and C. Mealli, *Dalton Trans.*, 2018, **47**, 17243–17256.
57 D. Tofan, Y. Sakazaki, K. L. Walz Mitra, R. Peng, S. Lee, M. Li and A. Velian, *Angew. Chem., Int. Ed.*, 2021, **60**, 8329–8336.
58 Y. Zhao, H. Wang, H. Huang, Q. Xiao, Y. Xu, Z. Guo, H. Xie, J. Shao, Z. Sun, W. Han, X.-F. Yu, P. Li and P. K. Chu, *Angew. Chem., Int. Ed.*, 2016, **55**, 5003–5007.
59 L. Wu, J. Wang, J. Lu, D. Liu, N. Yang, H. Huang, P. K. Chu and X.-F. Yu, *Small*, 2018, **14**, 1801405.
60 L. Chan, X. Chen, P. Gao, J. Xie, Z. Zhang, J. Zhao and T. Chen, *ACS Nano*, 2021, **15**, 3047–3060.
61 M. Fojtů, X. Chia, Z. Sofer, M. Masařík and M. Pumera, *Adv. Funct. Mater.*, 2017, **27**, 1701955.
62 S. P. Koenig, R. A. Doganov, L. Seixas, A. Carvalho, J. Y. Tan, K. Watanabe, T. Taniguchi, N. Yakovlev, A. H. Castro Neto and B. Özyilmaz, *Nano Lett.*, 2016, **16**, 2145–2151.
63 Z. Guo, S. Chen, Z. Wang, Z. Yang, F. Liu, Y. Xu, J. Wang, Y. Yi, H. Zhang, L. Liao, P. K. Chu and X.-F. Yu, *Adv. Mater.*, 2017, **29**, 1703811.
64 M. Vanni, M. Bellini, S. Borsacchi, L. Calucci, M. Caporali, S. Caporali, F. ďAcapito, M. Geppi, A. Giaccherini, A. Ienco, G. Manca, A. M. Mio, G. Nicotra, W. Oberhauser, M. Serrano-Ruiz, M. Banchelli, F. Vizza and M. Peruzzini, *J. Am. Chem. Soc.*, 2021, **143**, 10088–10098.
65 G. Abellán, V. Lloret, U. Mundloch, M. Marcia, C. Neiss, A. Görling, M. Varela, F. Hauke and A. Hirsch, *Angew. Chem., Int. Ed.*, 2016, **55**, 14557–14562.
66 P. Vishnoi, S. Rajesh, S. Manjunatha, A. Bandyopadhyay, M. Barua, S. K. Pati and C. N. R. Rao, *ChemPhysChem*, 2017, **18**, 2985–2989.
67 P. Vishnoi, M. Mazumder, M. Barua, S. K. Pati and C. N. R. Rao, *Chem. Phys. Lett.*, 2018, **699**, 223–228.
68 Y. Jing, Q. Tang, P. He, Z. Zhou and P. Shen, *Nanotechnology*, 2015, **26**, 95201.
69 X. Niu, Y. Li, Y. Zhang, Q. Li, Q. Zhou, J. Zhao and J. Wang, *J. Phys. Chem. Lett.*, 2018, **9**, 5034–5039.

70 R. Jain, Y. Singh, S.-Y. Cho, S. P. Sasikala, S. H. Koo, R. Narayan, H.-T. Jung, Y. Jung and S. O. Kim, *Chem. Mater.*, 2019, **31**, 2786–2794.
71 C. Su, Z. Yin, Q.-B. Yan, Z. Wang, H. Lin, L. Sun, W. Xu, T. Yamada, X. Ji, N. Zettsu, K. Teshima, J. H. Warner, M. Dincă, J. Hu, M. Dong, G. Su, J. Kong and J. Li, *Proc. Natl. Acad. Sci.*, 2019, **116**, 20844–20849.
72 C. Wang, D. Niu, B. Liu, S. Wang, X. Wei, Y. Liu, H. Xie and Y. Gao, *J. Phys. Chem.*, 2017, **121**, 18084–18094.
73 R. Gusmão, Z. Sofer and M. Pumera, *ACS Nano*, 2018, **12**, 5666–5673.
74 R. He, J. Hua, A. Zhang, C. Wang, J. Peng, W. Chen and J. Zeng, *Nano Lett.*, 2017, **17**, 4311–4316.
75 S. Wild, M. Fickert, A. Mitrovic, V. Lloret, C. Neiss, J. A. Vidal-Moya, M. Á. Rivero-Crespo, A. Leyva-Pérez, K. Werbach, H. Peterlik, M. Grabau, H. Wittkämper, C. Papp, H.-P. Steinrück, T. Pichler, A. Görling, F. Hauke, G. Abellán and A. Hirsch, *Angew. Chem., Int. Ed.*, 2019, **58**, 5763–5768.
76 A. Mitrović, S. Wild, V. Lloret, M. Fickert, M. Assebban, B. G. Márkus, F. Simon, F. Hauke, G. Abellán and A. Hirsch, *Chem. - Eur. J.*, 2021, **27**, 3361–3366.
77 M. G. Walter, E. L. Warren, J. R. McKone, S. W. Boettcher, Q. Mi, E. A. Santori and N. S. Lewis, *Chem. Rev.*, 2010, **110**, 6446–6473.
78 J. K. Nørskov, T. Bligaard, A. Logadottir, J. R. Kitchin, J. G. Chen, S. Pandelov and U. Stimming, *J. Electrochem. Soc.*, 2005, **152**, J23–J26.
79 J. Lu, X. Zhang, D. Liu, N. Yang, H. Huang, S. Jin, J. Wang, P. K. Chu and X.-F. Yu, *ACS Appl. Mater. Interfaces*, 2019, **11**, 37787–37795.
80 C. N. R. Rao and M. Chhetri, *Adv. Mater.*, 2019, **31**, 1803668.
81 S. Fukuoka, T. Taen and T. Osada, *J. Phys. Soc. Jpn.*, 2015, **84**, 121004.
82 T. Liang, Y. Liu, Y. Cheng, F. Ma and Z. Dai, *ChemCatChem*, 2020, **12**, 2840–2848.
83 W. Li, D. Liu, N. Yang, J. Wang, M. Huang, L. Liu, X. Peng, G. Wang, X.-F. Yu and P. K. Chu, *Appl. Surf. Sci.*, 2019, **467–468**, 328–334.
84 Y. Lin, Y. Pan and J. Zhang, *Int. J. Hydrogen Energy*, 2017, **42**, 7951–7956.
85 Z.-Z. Luo, Y. Zhang, C. Zhang, H. T. Tan, Z. Li, A. Abutaha, X.-L. Wu, Q. Xiong, K. A. Khor, K. Hippalgaonkar, J. Xu, H. H. Hng and Q. Yan, *Adv. Energy Mater.*, 2017, **7**, 1601285.
86 J. Wang, D. Liu, H. Huang, N. Yang, B. Yu, M. Wen, X. Wang, P. K. Chu and X.-F. Yu, *Angew. Chem., Int. Ed.*, 2018, **57**, 2600–2604.
87 T. Liang, Y. Liu, P. Zhang, C. Liu, F. Ma, Q. Yan and Z. Dai, *Chem. Eng. J.*, 2020, **395**, 124976.
88 X. Wang, L. Bai, J. Lu, X. Zhang, D. Liu, H. Yang, J. Wang, P. K. Chu, S. Ramakrishna and X.-F. Yu, *Angew. Chem., Int. Ed.*, 2019, **58**, 19060–19066.
89 R. Prasannachandran, T. V. Vineesh, M. B. Lithin, R. Nandakishore and M. M. Shaijumon, *Chem. Commun.*, 2020, **56**, 8623–8626.
90 T. Kosmala, L. Bardini, M. Caporali, M. Serrano-Ruiz, F. Sedona, S. Agnoli, M. Peruzzini and G. Granozzi, *Inorg. Chem. Front.*, 2021, **8**, 684–692.
91 D. Liu, J. Wang, J. Lu, C. Ma, H. Huang, Z. Wang, L. Wu, Q. Liu, S. Jin, P. K. Chu and X.-F. Yu, *Small Methods*, 2019, **3**, 1900083.
92 Y. Zhang, N. Dong, H. Tao, C. Yan, J. Huang, T. Liu, A. W. Robertson, J. Texter, J. Wang and Z. Sun, *Chem. Mater.*, 2017, **29**, 6445–6456.
93 X.-D. Zhu, Y. Xie and Y.-T. Liu, *J. Mater. Chem. A*, 2018, **6**, 21255–21260.
94 Y. Li, W. Pei, J. He, K. Liu, W. Qi, X. Gao, S. Zhou, H. Xie, K. Yin, Y. Gao, J. He, J. Zhao, J. Hu, T.-S. Chan, Z. Li, G. Zhang and M. Liu, *ACS Catal.*, 2019, **9**, 10870–10875.
95 J. Mei, T. He, J. Bai, D. Qi, A. Du, T. Liao, G. A. Ayoko, Y. Yamauchi, L. Sun and Z. Sun, *Adv. Mater.*, 2021, **33**, 2104638.
96 S. Suragtkhuu, M. Bat-Erdene, A. S. R. Bati, J. G. Shapter, S. Davaasambuu and M. Batmunkh, *J. Mater. Chem. A*, 2020, **8**, 20446–20452.
97 X. Song, B. Li, W. Peng, C. Wang, K. Li, Y. Zhu and Y. Mei, *Nanoscale*, 2021, **13**, 5892–5900.
98 T. Liang, S. Lenus, Y. Liu, Y. Chen, T. Sakthivel, F. Chen, F. Ma and Z. Dai, *Energy Environ. Mater.*, 2022, 1–10.
99 C. C. Mayorga-Martinez, N. Mohamad Latiff, A. Y. S. Eng, Z. Sofer and M. Pumera, *Anal. Chem.*, 2016, **88**, 10074–10079.
100 K. Pramoda, U. Gupta, M. Chhetri, A. Bandyopadhyay, S. K. Pati and C. N. R. Rao, *ACS Appl. Mater. Interfaces*, 2017, **9**, 10664–10672.
101 U. Maitra, U. Gupta, M. De, R. Datta, A. Govindaraj and C. N. R. Rao, *Angew. Chem., Int. Ed.*, 2013, **52**, 13057–13061.
102 P. Vishnoi, A. Sampath, U. V Waghmare and C. N. R. Rao, *Chem. - Eur. J.*, 2017, **23**, 886–895.
103 G. Zhao, T. Wang, Y. Shao, Y. Wu, B. Huang and X. Hao, *Small*, 2017, **13**, 1602243.
104 X. Zhu, T. Zhang, Z. Sun, H. Chen, J. Guan, X. Chen, H. Ji, P. Du and S. Yang, *Adv. Mater.*, 2017, **29**, 1605776.
105 W. Zhou, L. Dong, L. Tan and Q. Tang, *J. Phys. Chem.*, 2021, **125**, 7581–7589.
106 R. Marschall, *Adv. Funct. Mater.*, 2014, **24**, 2421–2440.
107 R. Boppella, W. Yang, J. Tan, H.-C. Kwon, J. Park and J. Moon, *Appl. Catal. B Environ.*, 2019, **242**, 422–430.
108 M. Zhu, S. Kim, L. Mao, M. Fujitsuka, J. Zhang, X. Wang and T. Majima, *J. Am. Chem. Soc.*, 2017, **139**, 13234–13242.
109 J. Ran, W. Guo, H. Wang, B. Zhu, J. Yu and S.-Z. Qiao, *Adv. Mater.*, 2018, **30**, 1800128.
110 Q. Zhang, S. Huang, J. Deng, D. T. Gangadharan, F. Yang, Z. Xu, G. Giorgi, M. Palummo, M. Chaker and D. Ma, *Adv. Funct. Mater.*, 2019, **29**, 1902486.
111 T. Song, L. Hou, B. Long, A. Ali and G.-J. Deng, *J. Colloid Interface Sci.*, 2021, **584**, 474–483.
112 J. Ran, B. Zhu and S.-Z. Qiao, *Angew. Chem., Int. Ed.*, 2017, **56**, 10373–10377.
113 J. Ran, X. Wang, B. Zhu and S. Z. Qiao, *Chem. Commun.*, 2017, **53**, 9882–9885.

114 Y.-J. Yuan, P. Wang, Z. Li, Y. Wu, W. Bai, Y. Su, J. Guan, S. Wu, J. Zhong, Z.-T. Yu and Z. Zou, *Appl. Catal. B Environ.*, 2019, **242**, 1–8.
115 L. Kong, Y. Ji, Z. Dang, J. Yan, P. Li, Y. Li and S. Frank Liu, *Adv. Funct. Mater.*, 2018, **28**, 1800668.
116 X. Cai, L. Mao, S. Yang, K. Han and J. Zhang, *ACS Energy Lett.*, 2018, **3**, 932–939.
117 B. Tian, B. Tian, B. Smith, M. C. Scott, R. Hua, Q. Lei and Y. Tian, *Nat. Commun.*, 2018, **9**, 1397.
118 M. Zhu, Z. Sun, M. Fujitsuka and T. Majima, *Angew. Chem., Int. Ed.*, 2018, **57**, 2160–2164.
119 J. Hu, D. Chen, Z. Mo, N. Li, Q. Xu, H. Li, J. He, H. Xu and J. Lu, *Angew. Chem., Int. Ed.*, 2019, **58**, 2073–2077.
120 D. A. Reddy, E. H. Kim, M. Gopannagari, Y. Kim, D. P. Kumar and T. K. Kim, *Appl. Catal. B Environ.*, 2019, **241**, 491–498.
121 M. Zhu, Y. Osakada, S. Kim, M. Fujitsuka and T. Majima, *Appl. Catal. B Environ.*, 2017, **217**, 285–292.
122 M. Zhu, X. Cai, M. Fujitsuka, J. Zhang and T. Majima, *Angew. Chem., Int. Ed.*, 2017, **56**, 2064–2068.
123 L. Mao, X. Cai, S. Yang, K. Han and J. Zhang, *Appl. Catal. B Environ.*, 2019, **242**, 441–448.
124 J. Wu, S. Huang, Z. Jin, J. Chen, L. Hu, Y. Long, J. Lu, S. Ruan and Y.-J. Zeng, *J. Mater. Sci.*, 2018, **53**, 16557–16566.
125 M. Zhu, C. Zhai, M. Fujitsuka and T. Majima, *Appl. Catal. B Environ.*, 2018, **221**, 645–651.
126 J. Hu, Y. Ji, Z. Mo, N. Li, Q. Xu, Y. Li, H. Xu, D. Chen and J. Lu, *J. Mater. Chem. A*, 2019, **7**, 4408–4414.
127 Q. Zhang, J. Zhang, L. Zhang, M. Cao, F. Yang and W.-L. Dai, *Appl. Surf. Sci.*, 2020, **504**, 144366.
128 S. Yılmaz, E. G. Acar, G. Yanalak, E. Aslan, M. Kılıç, İ. Hatay Patır and Ö. Metin, *Appl. Surf. Sci.*, 2022, **593**, 153398.
129 X. Ren, L. Shi, Y. Li, S. Song, Q. Wang, S. Luo, L. Ren, H. Zhang, Y. Izumi, X. Peng, D. Philo, F. Ichihara and J. Ye, *ChemCatChem*, 2020, **12**, 3870–3879.
130 R. Feng, K. Wan, X. Sui, N. Zhao, H. Li, W. Lei, J. Yu, X. Liu, X. Shi, M. Zhai, G. Liu, H. Wang, L. Zheng and M. Liu, *Nano Today*, 2021, **37**, 101080.
131 Y. Xu, X. Wang, M. Jin, K. Kempa and L. Shui, *ChemElectroChem*, 2020, **7**, 96–104.
132 X. Niu, Y. Li, H. Shu and J. Wang, *J. Phys. Chem. Lett.*, 2016, **7**, 370–375.
133 B. Jin, Y. Cho, C. Park, J. Jeong, S. Kim, J. Jin, W. Kim, L. Wang, S. Lu, S. Zhang, S. H. Oh, K. Zhang and J. H. Park, *Energy Environ. Sci.*, 2022, **15**, 672–679.
134 W. Li, Z. Wang, F. Zhao, M. Li, X. Gao, Y. Zhao, J. Wang, J. Zhou, Y. Hu, Q. Xiao, X. Cui, M. J. Eslamibidgoli, M. H. Eikerling, R. Li, F. Brandys, R. Divigalpitiya, T.-K. Sham and X. Sun, *Chem. Mater.*, 2020, **32**, 1272–1280.
135 C. Jellett, J. Plutnar and M. Pumera, *ACS Nano*, 2020, **14**, 7722–7733.
136 M. Barua, M. B. Sreedhara, K. Pramoda and C. N. R. Rao, *Chem. Phys. Lett.*, 2017, **683**, 459–466.
137 Z. Wu, Y. Lyu, Y. Zhang, R. Ding, B. Zheng, Z. Yang, S. P. Lau, X. H. Chen and J. Hao, *Nat. Mater.*, 2021, **20**, 1203–1209.